Materials Advances

ROYAL SOCIETY OF CHEMISTRY

REVIEW

View Article Online
View Journal | View Issue

Cite this: *Mater. Adv.*, 2023, 4, 2247

Received 27th December 2022,
Accepted 15th April 2023

DOI: 10.1039/d2ma01100j

rsc.li/materials-advances

Rational fabrication strategies of freestanding/binder-free electrodes for efficient capacitive deionization

Zhibo Zhao,[ab] Fangqiao Wang,[ab] Baobao Li,[ab] Zhuomin Chen,[ab] Hao Zhou,[ab] Xiaoru Wen*[c] and Meidan Ye *[ab]

Capacitive deionization (CDI) has received enormous attention as an emerging desalination alternative owing to the efficient energy footprint, low capital cost, and environmental friendliness. Conventionally, CDI electrodes are mainly fabricated using the slurry-coated method, through which insulated polymeric binders are utilized to integrate the active materials in powdery form and the conductive agents, thereby leading to inferior conductivity and poor cycling lifespan. Recently, freestanding/binder-free electrodes have provided great opportunities to improve the CDI performance due to the enhanced conductivity and stability. In this review, we show a comprehensive overview of the recent advances in the fabrication strategies (*e.g.*, template-free, template-guided, and other less-common methods) of freestanding electrodes for CDI. Besides, we also highlight the related deionization performance metrics, including the ion removal capacity, rates, efficiency, and energy consumption. Furthermore, we discuss the remaining challenges and further outlooks for the continued development of freestanding electrodes for CDI applications.

1. Introduction

Global population expansion, industrial explosion, and environmental pollution have caused overexploitation and utilization of freshwater resources. Hence, freshwater scarcity is currently one of the most concerning global crises faced by the human society.[1–3] It is worth noting that more than 97% of the water on Earth is seawater or brackish water,[4] making desalination one of the most effective and practical solutions to alleviate the growing demand for freshwater. Present-day,

---

[a] *Shenzhen Research Institute of Xiamen University, Shenzhen, 518057, China. E-mail: mdye@xmu.edu.cn*

[b] *Research Institute for Biomimetics and Soft Matter, Fujian Provincial Key Laboratory for Soft Functional Materials Research, Department of Physics, Xiamen University, Xiamen, 361005, China*

[c] *College of Chemistry and Chemical Engineering, Inner Mongolia University, Hohhot 010021, China. E-mail: xiaoru-wen@imu.edu.cn*

Zhibo Zhao

Zhibo Zhao received his B.S. in College of Chemistry and Chemical Engineering from Inner Mongolia University, China in 2022. He is now a graduate student in the College of Physical Science and Technology, Xiamen University, China. He joined Professor Meidan Ye's group in 2022. His research focuses on energy storage materials and devices.

Fangqiao Wang

Fangqiao Wang received his B.S. in College of Materials from Fujian University of Technology, China in 2021. He is now a graduate student in the College of Physical Science and Technology, Xiamen University, China. He joined Professor Meidan Ye's group in 2021. His research focuses on energy storage materials and devices.

large-scale water purification technologies mainly use thermal processes or membrane-based desalination, which mostly include multi-stage flash (MSF),[5] multi-effect distillation (MED),[6] reverse osmosis (RO),[7] and electrodialysis (ED).[8] However, most of the conventional desalination systems have limitations, including considerable energy consumption and secondary pollution. Thermal desalination requires large amounts of thermal energy to separate water vapor.[9] RO is a process that needs high pressure to exceed the osmotic pressure of the feed solution.[9,10] What is more, the extremely high voltage, utilized for the migration of salt ions during the ED processes, could cause water decomposition.[9,11] Consequently, sustainable technologies for water remediation with lower energy implementation, high efficiency, and zero secondary waste are urgently required.

Capacitive deionization (CDI), burgeoned with the properties of efficient energy footprint, low capital cost, and environmental friendliness, has attracted enormous attention as a promising next-generation desalination alternative.[12–15] Different from traditional desalination technologies, CDI generally does not require the thermal treatment, sophisticated membrane, or an extremely high applied voltage, but relies on extracting exotic species from the feed stream through electric charges at room temperature. Typically, the ions induced by the external electrostatic field (normally < 2.0 V) between a pair of fixed electrodes migrate oppositely to the charged electrodes.[16–21] Subsequently, the charged ions are immobilized within the electrodes, producing freshwater (Fig. 1a). The stored ions can be released back into the bulk solution by eliminating or reversing the applied voltage, further refreshing the electrodes and inverting the deionization process (Fig. 1b). Thus, the electrodes, as a core part of CDI, play a decisive role in efficient deionization.

Generally, CDI electrode materials are conceptually categorized into non-Faradaic *via* the electrosorption/electrical double layer (EDL) mechanism and Faradaic materials harnessing the underpinning surface redox, ion insertion, or conversion reaction processes (Fig. 1c and d).[2,22,23] Carbon materials, predominantly based on electrosorption mechanisms, have been vigorously explored as traditional CDI electrodes due to the merits of good electrical conductivity, adjustable porous structure, and electrochemical stability.[24–30] However, the utilization of carbon materials remains precluded by the moderate removal capacity, inevitable co-ion expulsion, and non-permselective counterion capture in high molar strength.[31,32] Unlike carbon-based materials, Faradaic materials enable ions to be trapped accomplished by the charge transfer process within the bulk electrodes through the abovementioned reactions, which gives them a higher deionization capacity, tolerability, and permselectivity at a high ionic concentration.[33–38] Therefore, Faradaic materials have been rigorously adopted to ameliorate the aforementioned limitations of carbon-based materials in the CDI community, triggered by the pioneering work of a desalination battery, hybrid CDI, and intercalation-based systems.[39–41]

Until now, prosperous deployment of CDI mostly dedicates on leveraging state-of-the-art electrode materials ranging from tailoring carbon materials (*e.g.*, porosity,[42] surface area,[43] and surface functionalization[44,45]) to exploiting various Faradaic materials (*e.g.*, metal oxides,[46–48] MXene,[49] transition metal dichalcogenides (TMDs),[50] carbon/Faradaic compositions,[51–53] and so on). However, innovation in the fabrication of electrodes for CDI also shows substantial potential. In general, most

Baobao Li

Baobao Li received his B.S. in College of Physical Science and Technology from Guangxi University, China in 2021. He is now a graduate student in the College of Physical Science and Technology, Xiamen University, China. He joined Professor Meidan Ye's group in 2021. His research focuses on 2D-energy storage materials and devices.

Xiaoru Wen

Xiaoru Wen received her PhD from the College of Chemistry and Chemical Engineering at Xiamen University in 2017. She then joined the College of Chemistry and Chemical Engineering of Inner Mongolia University as a lecturer in 2017. She was promoted to associate Professor in 2021. Her research interests are in multi-functional materials for water-treatment devices, i.e., capacitive deionization.

Meidan Ye

Meidan Ye received her PhD from the College of Chemistry and Chemical Engineering at Xiamen University in 2014. She then joined the Research Institute for Soft Matter and Biomimetics, Department of Physics, College of Physical Science and Technology at Xiamen University as an associate Professor in 2014. She was promoted to a Professor in 2021. Her research interests are in multi-functional materials for flexible devices, i.e., electrochemical energy storage devices and wearable sensors.

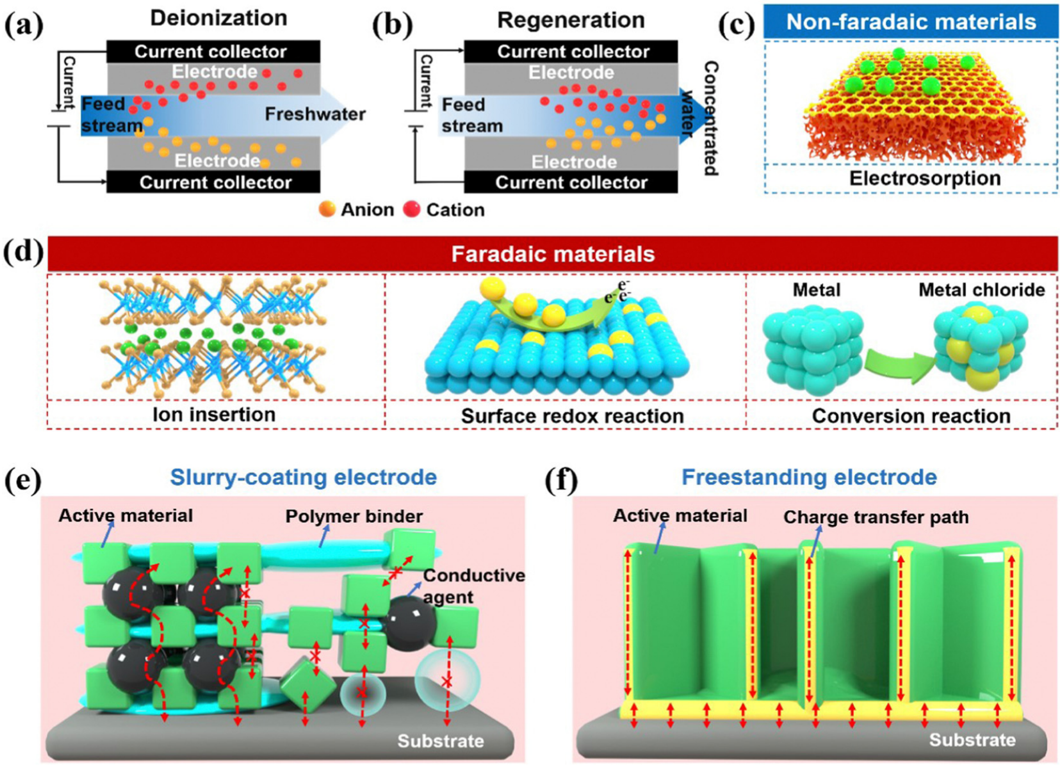

Fig. 1 Schematic illustration of the (a) deionization process, (b) regeneration process, ion uptake mechanisms of (c) non-Faradaic materials and (d) Faradaic materials, and specific features of a (e) slurry-coating electrode and (f) freestanding electrode.

conventional electrodes are prepared based on the indispensable slurry-coated method, in which the mixed slurries of active materials, conductive agents (*e.g.*, carbon black), and polymeric binders with a typical ratio of 8 : 1 : 1 are cast onto a current collector.[54,55] During this process, polymeric binders (*e.g.*, polytetrafluoroethylene (PTFE) and polyvinylidene (PVDF)) are implemented to integrate each individual component. Unfortunately, polymeric binders are generally inactive and hydrophobic, which inevitably deplete the electrical conductivity, deteriorate the capacity performance, and increase the cost (Fig. 1e).[56] Significant research has been conducted to study and enhance the electrical conductivity of slurry-coated electrodes.[57–59] Moreover, the poor adhesion force between the cast materials and the substrates leads to inferior cycling stability,[60] in which the active materials can be easily dislodged from the conductive substrates during the long-term deionization process. Therefore, it is imperative to replenish radical preparation methods to avoid the utilization of detrimental binders. In recent years, binder-free electrodes have attracted substantial attention due to the following metrics. First, non-binder preparation methods without the post-coating process, addition of polymeric binders, and conductive additives can simplify the electrode fabrication procedures and lower the manufacturing costs.[61] Second, most binder-free electrodes are attached directly onto the conductive matrix by the judicious *in situ* methods, in which the intimate binding and seamless contact between active phases and substrates can consolidate the effective charge transfer and suppress the active mass shedding (Fig. 1f).[62] Third, the adsorbed ions in the bulk stream can sufficiently access active space and facilitate mass transfer without the insulation of polymeric binders. Thus, the binder-free electrodes favor enhancing the deionization performance and cycling stability for practical high-performance CDI. Considering the substantial development achieved in binder-free electrodes for CDI, it is essential to review the progress and outlooks in recently reported advanced binder-free electrodes.

In this review, we intend to focus on various recent fabrication methods of the freestanding (mostly binder-free) electrodes utilized in CDI, mainly including template-free, template-guided methods and some others (Fig. 2 and Table 1). Herein, the freestanding electrode demonstrates the active materials freely stand/attach on the conducive substrate without the assistance of polymeric additives, featuring a self-supported characteristic. Moreover, electrospinning, vacuum filtration, and paste-molding methods are the main template-free methods, which usually integrate active materials together or with conductive carbon-based materials. Among the template-guided methods, *in situ* growth strategies (*e.g.*, hydrothermal/solvothermal methods, chemical bath deposition, and thermal treatment) are exploited to prepare freestanding electrodes on the conductive supporting substrates (*e.g.*, Ni foam, Ti plate, carbon cloth, graphite paper, and wood). And some other less-common technologies in the CDI field, such as 3D printing, electrophoretic deposition, and so on, are also summarized. Meanwhile, we also highlight and investigate the electrochemical and deionization performance metrics, such as ion removal capacity, efficiency,

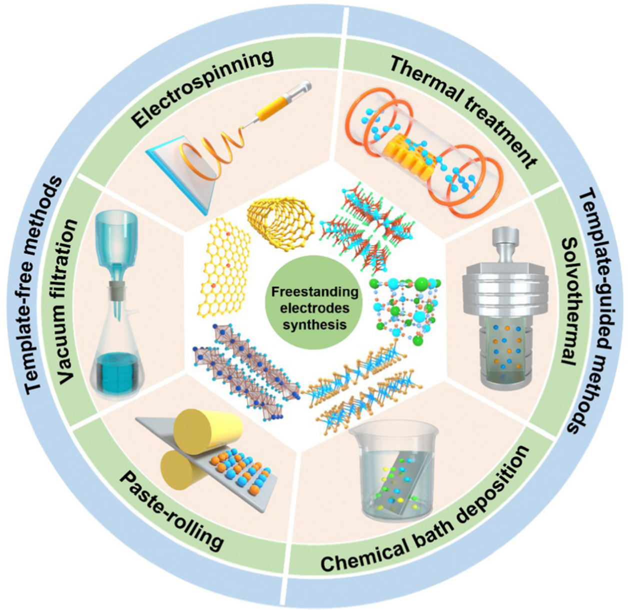

Fig. 2 Schematic diagrams of the active materials, template-free, and template-guided fabrication methods of the freestanding electrodes.

energy consumption, and rates in the CDI application. Finally, we critically discuss the challenges and perspectives for the further development of freestanding electrodes in the CDI community.

2. CDI performance evaluation metrics

Establishing systematic CDI performance metrics is substantial in the evaluation of deionization performances of electrodes, which are utilized for various CDI cell architectures. In term of CDI cell configurations, versatile cell-architecture concepts, ranging from the conventional cell designed in the original CDI to the further hybrid CDI (HCDI) and ion-exchange membrane (IEM)-based CDI (*e.g.*, flow electrode CDI and rocking-chair CDI), have been explored with the development of CDI.[2,13,63] Albeit at different cell configurations, the underlying processes decoupled from all architectures, in which the target cations and anions are immobilized by cathode and anode electrodes through the invested charges under external voltages, respectively, are in essence the same. The real-time conductivity of the bulk feed stream is recorded by a conductivity meter throughout the deionization process. Moreover, the voltages and dynamic currents supplied by the direct current (DC) power meter are recorded by a battery analyzer for further utilization. Beyond the cell design described above, other variable factors such as operational parameters including the initial solution concentration, applied voltage, flow rate, and ion type, can indispensably affect the CDI performance. Correspondingly, the related key evaluation metrics are presented in the following chapters.

2.1. Ion/salt removal capacity

Ion removal capacity is one of the most intuitive performance metrics used to evaluate the deionization capability, which denotes the number of ions removed from the feed bulk solution. The salt removal capacity depends on the process by which ionic species (*e.g.*, cations and anions) compensate for the depleted charges of electrodes, so it is rational to normalize the deionization capacity by the electrode mass. Thus, the gravimetric salt removal capacity, defined as the mass of ions removed per unit mass of electrode ($\mathrm{mg_{ions}\ g^{-1}{}_{electrodes}}$), is calculated by eqn (1):[14]

$$\text{Ion removal capacity} = \frac{(C_0 - C_t)V}{m} \tag{1}$$

where C_0 and C_t are the initial and final concentrations of the streaming ion solution ($\mathrm{mg\ L^{-1}}$), respectively. V depicts the total rotative volume of the feed solution (L), and m represents the total mass of the paired electrodes (g).

Additionally, the ion release capacity during the electrode regeneration or long-term cycling process, which can inevitably deviate from deionization capacity, is also a substantial signature. Specifically, the release capacity, demonstrating the resilience of electrodes, is a critical diagnostic metric to estimate electrode performance and system condition.[2]

2.2. Ion/salt removal rate

In addition to the ion removal capacity, the salt removal rate, reflecting the rate of deionization (or electrode regeneration) process,[64,65] is another important metric to be considered using eqn (2):

$$\text{Ion removal rate} = \frac{\text{Ion removal capacity}}{t} \tag{2}$$

where t is the corresponding deionization time ($\mathrm{s\ min^{-1}}$). As defined, the unit of ion removal rate is $\mathrm{mg\ g^{-1}\ s^{-1}/mg\ g^{-1}\ min^{-1}}$.

Similar to the deionization capacity, the deionization rate also depends highly on factors including the electrode materials (*e.g.*, intrinsic kinetics), electrode fabrication (*e.g.*, thickness), cell architectures (*e.g.*, flow by and flow through), and operational parameters (*e.g.*, flow rates and influent concentrations).[66,67]

2.3. Charge efficiency

Charge efficiency (Λ) is defined as the ratio of the amount of removed species from the feed stream and the total invested electric charges during the ion removal process,[68,69] as described in eqn (3):

$$\text{Charge efficiency}(n) = \frac{(C_0 - C_t)VF}{M\int_0^t I\mathrm{d}t} \tag{3}$$

where F is the Faraday constant ($96\,485\ \mathrm{C\ mol^{-1}}$), M is the molar mass of removed species (*e.g.*, NaCl/58.44 $\mathrm{g\ mol^{-1}}$) and I is the real-time current recorded by the analyzer.

Ideally, the total invested electric charges are utilized to extract ions, in which the value of charge efficiency could approach 1. However, there are several detrimental factors that suppress the energy utilization, including the exacerbated co-ion expulsion in high concentrations, especially for carbon electrodes, and adverse side reactions.[70,71]

Table 1 Freestanding electrodes with their corresponding synthetic methods and deionization performance

Electrodes	Methods	Ion removal capacity	Cycling stability	Ref.
Co_3O_4@CNF@CNT	Electrospinning with annealing and oxidization	56.86 mg g^{-1} in a NaCl solution of 1500 mg L^{-1} at 1.2 V	Negligible deterioration after 20 cycles	88
CNF@Mn_2O_3	Electrospinning with a chemical bath	27.43 mg g^{-1} in a NaCl solution of 3000 mg L^{-1} at 1.2 V	14.3% decay in 30 cycles	91
S,N co-doped CNT	Electrospinning with thermal treatment	29.50 mg g^{-1} in a 500 mg L^{-1} NaCl solution at 1.4 V	Slight fluctuation during 23 cycles	89
Graphene quantum dots decorated CNT	Electrospinning with thermal and etch treatment	19.34 mg g^{-1} in a 500 mg L^{-1} NaCl solution at 1.2 V	94% capacity retention after 30 cycles	90
N-CNF P-CNF	Electrospinning with annealing treatment	30.4 mg g^{-1} in a 500 mg L^{-1} NaCl solution at 1.2 V	Over 70 cycles	92
Graphene embedded with fungal hyphae	Vacuum filtration with calcination treatment	32.3 mg g^{-1} in a 10 mM NaCl solution at 1.2 V	Less than 5% decay after 50 cycles	105
Porous carbon pad	Vacuum filtration with carbonization and activation processes	35.6 mg g^{-1} in a 585 mg L^{-1} NaCl solution at 1.2 V	Variation less than 10% after 40 cycles	106
MXene/NiHCF	Vacuum filtration with chemical bath	85.1 mg g^{-1} in a 1000 mg L^{-1} NaCl solution at 1.4 V	No obvious degradation after 50 cycles	112
CoFe-LDH/MXene	Vacuum filtration	149.25 ± 6.17 mg g^{-1} in a NaCl solution of 20 mM at 50 mA g^{-1}	Capacity retention of 81.7% after 30 cycles	113
Na^+–$Ti_3C_2T_x$-MS	Paste-rolling with molten-salt process	14.8 mg g^{-1} in a NaCl solution of 100 mg g^{-1} at 1.2 V	90.5% after 10 cycles	119
N-doped graphene	Compression molding	21.8 mg g^{-1} in a NaCl solution of 100 mg g^{-1} at	Retention of 95% after 10 cycles	115
WS_2/rGO-CNT aerogel	Solvothermal with freeze-drying	80 mg g^{-1} in a 3000 mg L^{-1} NaCl solution at 1 mA	Over 50 cycles	131
VS_2@GP	Hydrothermal	31.19 mg g^{-1} in a 520 mg L^{-1} NaCl solution at 1.2 V	Without evident degradation after 30 cycles	132
MoS_2/CoS_2@TiO_2	Hydrothermal with electrodeposition	44.22 mg g^{-1} in a 600 mg L^{-1} NaCl solution at 1.2 V	A subtle decay after 20 cycles	124
Nano-patterned MOF	Chemical bath deposition	21.3 mg g^{-1} in a 40 mM NaCl solution at 1.2 V	Little capacity fading after 30 cycles	141
rGO/CNF	Chemical bath deposition	84.6 mg g^{-1} in a 250 mg L^{-1} NaCl solution at 1.2 V	Over 91% capacity retention after 20 cycles	142
N-doped CNT	Chemical bath deposition with etch and pyrolysis treatment	56.9 mg g^{-1} in a 60 mM NaCl solution at 1.2 V	Little capacity fading after 50 cycles	143
Balsa wood	Thermal treatment with etch process	12.45 mg g^{-1} in a 500 mg L^{-1} NaCl solution at 1.2 V	No obvious decline after 12 h	146
Mg^{2+}-MXene aerogel	Sol–gel with freeze-drying	33.3 mg g^{-1} in a 1000 mg L^{-1} NaCl solution at 1.4 V	Over 30 cycles	159
MXene/CNT	Electrodeposition	34.5 mg g^{-1} in a 500 mg L^{-1} NaCl solution at 1.2 V	Retention of 89% after 40 cycles	161
N-doped GO/CNT	3D printing	75 mg g^{-1} in a 2500 mg L^{-1} NaCl solution at 100 mA g^{-1}	50 cycles	167

2.4. Energy consumption

Energy consumption of deionization is a radical metric to differentiate from other traditional water remediation technologies with the exclusive future of efficient energy footprint. Generally, in the CDI community, the energy consumption is expressed as the specific energy consumption, which is assigned to the energy spent per unit amount of removed species (such as the terms of W h g^{-1} and J mol^{-1}).[72,73] The energy consumption is drastically susceptible to various operational parameters, such as the stream concentration, working mode (constant voltage *vs.* constant current), and the charge efficiency.[74,75] Furthermore, according to the aforementioned definition, the energy consumption is usually given by eqn (4):

$$\text{Energy consumption} = \frac{\int_0^t UI\mathrm{d}t}{(C_0 - C_t)V} \qquad (4)$$

where U and I are the voltage (V) and current (A), respectively, and the unit of the calculated energy consumption is W h g^{-1}.

3. Template-free methods for the fabrication of freestanding CDI electrodes

Generally, template-free methods, mostly including electrospinning, vacuum filtration, paste rolling, and paste molding, can directly fabricate freestanding CDI electrodes without the assistance of substrates but usually with further combinational treatment. Moreover, the freestanding electrodes prepared using template-free methods are mainly nanofibers and film-forming electrodes without constraint of templates, thereby giving it flexibility, controllability, and tunability.

3.1. Electrospinning

Electrospinning technology, featuring controllability, simplicity, and high efficiency, has attracted enormous attention as a promising strategy to prepare one-dimensional (1D) nanofibers with tunable diameters.[76,77] Furthermore, it is one of the most exceptional methods used to fabricate freestanding electrodes, mostly consisting of randomly interconnected nanofibers. Fig. 3a displays the general setup of an electrospinning unit including a high voltage power supply, a spinneret, and a conductive fiber collector. Typically, the conductive precursor solution filled in the spinneret is firstly charged under the sufficiently high voltage applied between the paired spinneret and the collector. Afterwards, the liquid tip will be gradually tailored into a conical shape called the Taylor cone associated with the counteraction between the electrostatic repulsive forces and the surface tension. When the increasing electrostatic repulsion overcomes the surface tension, the droplet ejects a stream of charged liquid flying towards the collector. Finally, the solidified nanofibers gathered on the collector are obtained from the charged jet after the complex stretching and elongating motion in conjunction with the evaporation of solvent during the free flying process.[78] Clearly, the precursor, polymer or melt, plays a vital role in the electrospinning technology. Generally, different polymers exhibit different chain entanglements in the precursor solutions, which could influence the diameters of the as-fabricated nanofibers. Moreover, materials including metal, metal oxide, ceramics, and combinations can be made into nanofibers with post-treatment, in which the pretreated polymeric precursor has the suitable properties (*e.g.*, conductivity, viscosity, and surface tension) for electrospinning.[79–82]

Furthermore, it is worth noting that most of the freestanding CDI electrodes synthesized by electrospinning with a subsequent thermal process are stable and conductive carbon-based nanofibers decomposed from various polymers (typically, polyacrylonitrile (PAN)). Therefore, the development of electrospun nanofibers for freestanding CDI electrodes progressively encompasses modifying texture properties (such as porosity and hydrophilicity) and exploiting hybrid electrodes. Specifically, ZnO/N-doped porous carbon fibers,[83] MnO_2/rGO-doped PAN composite fibers,[84] activated carbon fibers (ACF),[85] carbon nanofiber (CNF) hybrids,[86] and NiO-doped carbon nanofibers[87] have been successfully fabricated *via* electrospinning with post-treatments.

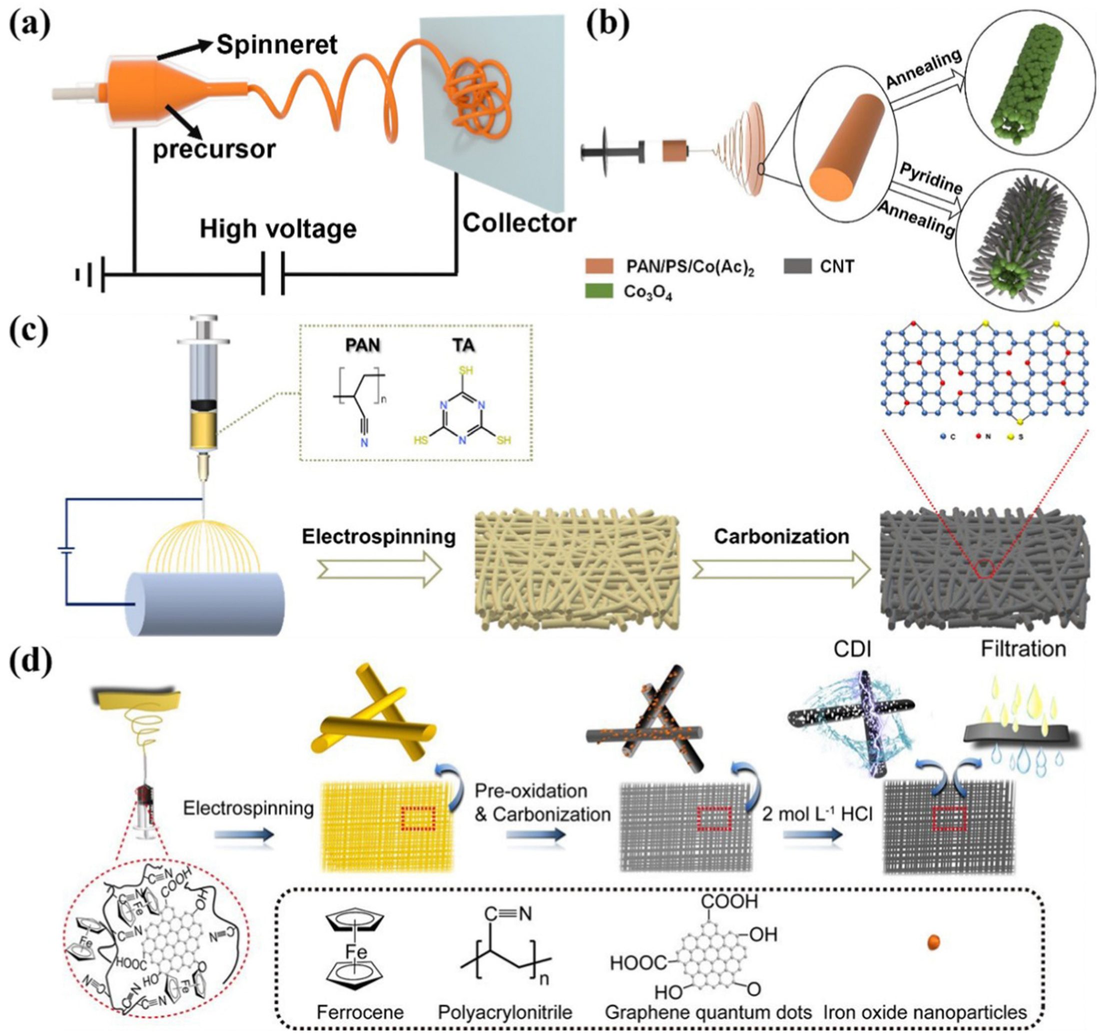

Fig. 3 (a) Schematic diagrams of the electrospinning process. Illustration of the preparation of the freestanding (b) Co_3O_4@CNF@CNT and (c) S/N co-doped CNT electrodes, reproduced from ref. 88 and 89 with permission from Elsevier. (d) Schematic of the fabrication of graphene quantum dot modified CNT electrodes, reproduced from ref. 90 with permission from the American Chemical Society.

Embedding carbon nanofibers with Faradaic materials is an effective way to prepare the freestanding electrodes using electrospinning-based strategies. For instance, Guo *et al.*[88] used a specific precursor to prepare freestanding Co_3O_4/CNT decorated nanofibers (Co_3O_4@CNF@CNT) using an electrospinning-annealing-oxidization procedure. Specifically, during the thermal process, the tubular carbon nanofibers were constructed without any residual polymeric additives under the decomposition and evaporation of polystyrene (PS), thereby providing the freestanding electrodes with a conductive network. And the nitrogen doped CNTs were embedded by bubbling pyridine, in which pyridine and Co_3O_4 worked as the carbon source and catalyst, respectively. As shown in Fig. 3b, CNT tentacles encapsulating the CNF matrix anchored with Co_3O_4 nanoparticles can be clearly observed. And the conductive CNF substrate and N-doped CNT tentacles improved the electrical conductivity and favored the hydrophilicity, permeability, and electrochemical performance. Therefore, the as-prepared Co_3O_4@CNF@CNT based HCDI cell delivered a satisfactory SAC (*i.e.*, 58.6 mg g^{-1} in a NaCl solution of 1500 mg L^{-1}) associated with an excellent salt adsorption rate (SAR, 12.27 mg g^{-1} min^{-1} in a NaCl solution of 2500 mg L^{-1}) at 1.4 V.

Furthermore, the HCDI system achieved reliable durability with no obvious deterioration after 20 cycles. In addition, Liu *et al.*[91] reported freestanding Mn_2O_3 decorated electrospun carbon nanofibers (CNF@Mn_2O_3) using electrospinning and subsequent *in situ* chemical bath methods. The Faradaic Mn_2O_3 nanoflowers coated on the 1D CNFs can provide exceptional pseudo-capacitance to the CDI system, in which the CNF@Mn_2O_3 based HCDI system demonstrated superior SAC (27.43 mg g^{-1}), stability (14.3% decay in 30 cycles), and charge efficiency (0.92) in a NaCl solution with the initial concentration of 3000 mg L^{-1} under an applied voltage of 1.2 V.

Apart from the integration of carbon nanofibers and advanced Faradaic materials, the heteroatom doping strategy can also be fabricated through the electrospinning-based methods and serve as freestanding electrodes without any conductive additive and polymer binder. For instance, Gao *et al.*[89] fabricated S,N co-doped carbon nanofibers directly utilized as a freestanding CDI electrode by the co-electrospinning method coupled with a thermal treatment. As schematically illustrated in Fig. 3c, trithiocyanuric acid (TA) and PAN acted as the S/N and carbon sources, respectively, during the carbonization treatment. The obtained S,N co-doped carbon nanofibers provided high electrical conductivity, improved hydrophilicity, and tailored pore structures, which were derived from an electron-rich heteroatom (S, N) doping strategy and conductive carbon backbone under the decomposition of polymeric additives. Large specific surface area (523 m^2 g^{-1}), better wettability, and integrated binder-free structures led to a satisfactory salt adsorption capacity (SAC) of 29.50 mg g^{-1} in a 500 mg L^{-1} NaCl solution under an applied voltage of 1.4 V. The superior charged efficiency ($>80\%$) and cycling stability (slight fluctuation during 23 cycles) were also demonstrated. Moreover, their theoretical calculations indicated the synergistic effect of S,N co-doping on boosting the adsorption capacity of both Na and Cl ions.

Additionally, leveraging the texture properties including porosity, surface area, and surface functionalization of carbon nanofibers is also a preferential strategy to synthesize electrospinning-based freestanding electrodes. Gong *et al.*[90] contrived a porous hydrophilic carbon nanofiber fabric decorated with graphene quantum dots as a freestanding electrode by electrospinning in combination with thermal and etch treatment. Notably, as displayed in Fig. 3d, the authors integrated the metrics of electrospinning (*e.g.*, structural tunability and composition modulation), in which the well-designed porous structure and hydrophilicity were produced from the pore and hydrophilic groups formerly dissolved in the polymer precursor. Moreover, the polymeric additives were decomposed into a conductive carbon matrix effectively, which could eliminate the deleterious influence of the insulated polymeric additives during the carbonization process. And the interconnected mesoporous structure and good hydrophilicity in conjunction with the large accessible surface area (405 m^2 g^{-1}) of the as-prepared monolithic binder-free fabric are favorable for the hydrated Na^+ and Cl^- ion adsorption, enabling a superior desalination capacity of 19.34 mg g^{-1} at 1.2 V in a 500 mg L^{-1} NaCl solution associated with good cycling stability (94% capacity retention after 30 cycles). In another recent study, Nie *et al.* fabricated the opposite surface charged carbon nanofibers as a self-supporting electrode for the inverted CDI, using electrospinning with subsequent annealing treatment.[92] The negative charged carbon nanofibers (N-CNF) and positive charged carbon nanofibers (P-CNF) were dramatically exploited as the cathode and anode, respectively, which was termed inverted CDI. Moreover, numerous vacated active sites were liberated under the pre-charging activation process, in which ions were individually adsorbed followed by desorption driven by the voltage difference between N-CNF and P-CNF, leading to the delivery of an outstanding desalination capacity of 30.4 mg g^{-1} with a satisfactory desalination rate (1.0 mg g^{-1} min^{-1}). The experimental results unveiled the superior cycling durability over 70 cycles.

In short, although the electrospinning method is suitable for synthesizing freestanding CDI electrodes, it is imperative to explore effective but simple design routes of polymer type, concentration, and material properties, along with the subsequent property–performance relationship between nanofibers and desalination capacity. Furthermore, coupling with more categories of Faradaic materials and integrating more subsequent post-treatment procedures remains challenging.

3.2. Vacuum filtration

Vacuum filtration is an effective and facile strategy to prepare freestanding films serving as monolithic electrodes, featured with good homogeneity, flexibility, and controllable thickness.[93,94] Generally, as depicted in Fig. 4a, the pre-treated solution or dispersion is filtered through the specific membrane, in which the target materials uniformly accumulate and stack on the membrane surface, forming a macroscopic film. Furthermore, no polymeric additives are generally required to construct the monolithic electrodes by vacuum filtration. Thus, various flexible freestanding CDI electrodes, such as carbon-based and twodimensional (2D)-based materials, can be fabricated by filtering different specific precursors. Typically, carbon-based materials (especially carbon nanotubes (CNTs), activated carbon (AC), and graphene), possessing features of excellent electrical conductivity, large specific surface area, and exceptional mechanical stability, have received substantial attention as ideal supports in the energy storage community.[95,96] Therefore, vacuum filtration is commonly utilized to couple the aforementioned carbon-based materials with other outperformed materials to form integrated freestanding electrodes (*e.g.*, TiS_2/CNT,[97] MoS_2/CNT,[98] V_2O_5/CNT,[99] $Na_3V_2(PO_4)_3$ (NVP)/CNT,[100] MXene/AC,[101] $Na_2Ti_3O_7$-CNT (NCNT)@rGO,[102] MXene-derived sodium titanate (M-NTO)/rGO,[103] and N-doping graphene (NDG) paper[104]) for high performance CDI.

For example, Chen *et al.*[105] embedded graphene with binder-free fungal hyphae derived from *Aspergillus niger* (G-FhEld) to form the freestanding pad, by a facile vacuum filtration process with subsequent calcination treatment (Fig. 4b). The fabricated G-FhEld pad was directly utilized as the freestanding CDI electrode without any binders or conductive additives. The interwoven fibers sintered from fungal hyphae provided a conductive 3D carbon backbone with a hierarchical structure for CDI. Moreover, the embedment of graphene enhanced the electrical conductivity, increased the specific surface area, and provided extra available active sites for target ions, which synergistically improved the salt storage performance. As a result, the freestanding electrode realized a SAC of 32.3 mg g^{-1} associated with an average removal rate of 1.1 mg g^{-1} min^{-1} and a high current efficiency (96.2%) in a low-salinity concentration of 10 mM under an applied voltage of 1.2 V. Also, the variation of SAC was less than 5% after 50 CDI cycles, demonstrating the superb long-term stability. Moreover, in another recent biological material work, Chen *et al.*[106] obtained the freestanding porous carbon pad derived from fungal hypha *via* the vacuum filtration method followed by carbonization and activation processes. The fungal hypha activated carbon pad (FhACPad) film consisting of interconnected fibers can be cut into a specific size and directly utilized as the electrode because of its flexibility and integrity. The freestanding FhACPaD realized a desalination capacity of 35.6 mg g^{-1} with a removal rate of

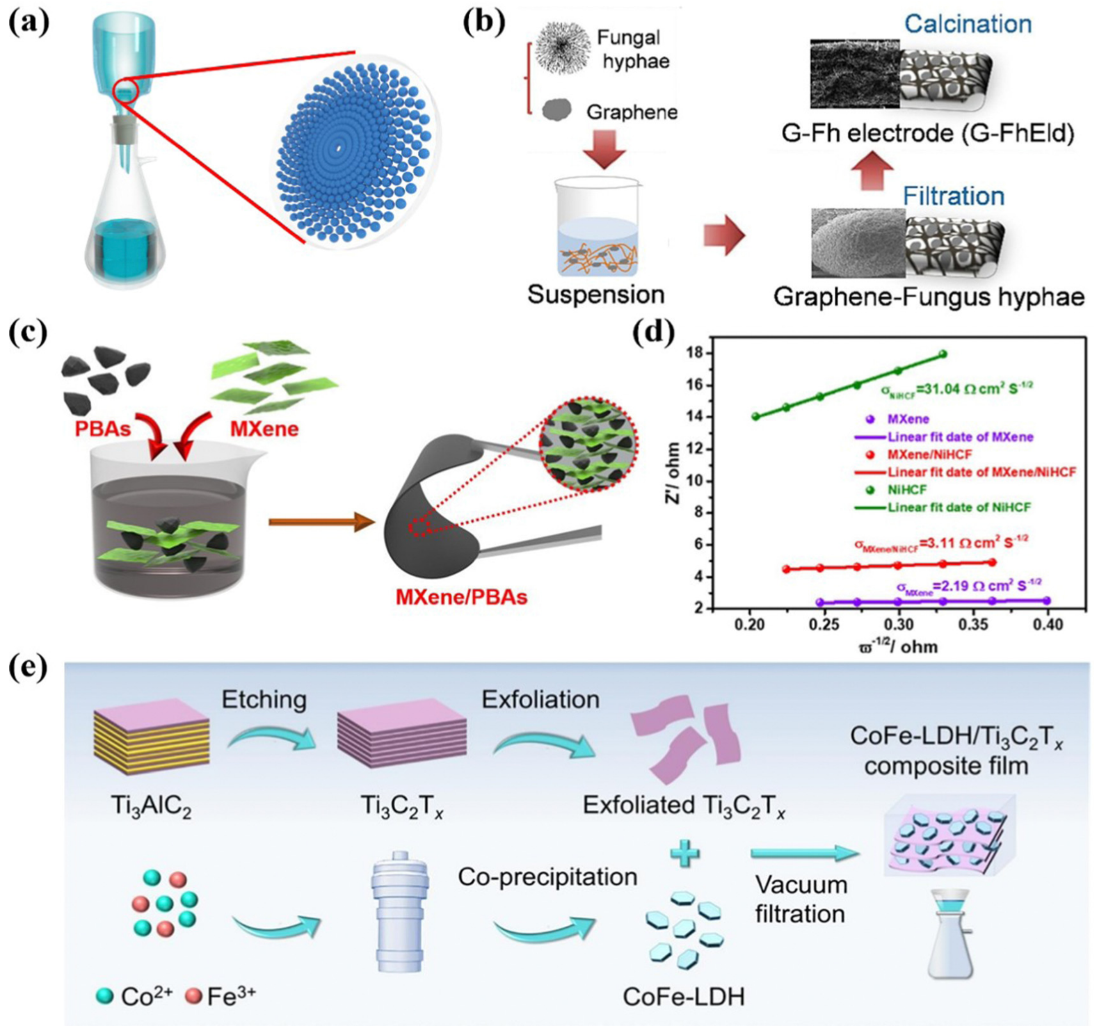

Fig. 4 (a) Schematic illustration of vacuum filtration. Schematic diagram of (b) preparation of a graphene-fungus hyphae electrode, (c) fabrication and (d) Z' *vs.* frequency ($\omega^{-1/2}$) of the freestanding MXene/Prussian blue analogues electrodes, and (e) CoFe-LDH/MXene synthesis. Reproduced from ref. 105 and 113 with permission from Elsevier, and reproduced from ref. 112 with permission from American Chemical Society.

1.2 mg g^{-1} min^{-1}, which was much higher than the traditional slurry-casted AC electrode.

Additionally, MXenes, benefiting from its accessible sandwich-like feature, extraordinary theoretical electrochemical capacity, and facile ion intercalation/deintercalation, have been vigorously exploited as prospective Faradaic candidates for the rational construction of freestanding CDI electrodes by the vacuum filtration method. For instance, L-S-$Ti_3C_2T_x$ films,[107] Ag/$Ti_3C_2T_x$,[108] three-dimensional (3D) alkalized $Ti_3C_2T_x$,[109] freestanding $Ti_3C_2T_x$ films,[110] and $Ti_3C_2T_x$/bacterial fibers (BC)[111] have been successfully fabricated for CDI applications. For instance, Wang *et al.*[112] designed freestanding $Ti_3C_2T_x$ films with embedded Prussian blue analogues (PBAs, specially nickel hexacyanoferrate (NiHCF) and copper hexacyanoferrate (CuHCF)) particles, which were directly utilized as HCDI electrodes, *via* the vacuum filtration strategy. The scanning electron microscopy (SEM) image of $Ti_3C_2T_x$/PBAs films (Fig. 4c) indicated the PBAs nanoparticles were encapsulated in the $Ti_3C_2T_x$ nanosheets. The embedded NiHCF/CuHCF nanoparticles can not only restrain the restacking of $Ti_3C_2T_x$ nanosheets, but also enlarge the interlayer spacing, thus replenishing more accessible active surface areas and forming more opening structures, which were preferential for the ion diffusion and intercalation. Moreover, the conductive $Ti_3C_2T_x$ nanosheets embedded with the PBA particles forming a 3D conductive framework in turn effectively improved the desalination kinetics and consolidated the electron transmission throughout the electrodes. The significantly decreased slope of $Ti_3C_2T_x$/NiHCF (Fig. 4d) demonstrated the improved Na^+ ion diffusion owing to the conductive $Ti_3C_2T_x$. Benefiting from the synergistic effect of MXene, PBAs, and binder-free preparation, the freestanding $Ti_3C_2T_x$/NiHCF films showed an ultrahigh desalination capacity of 85.1 mg g^{-1} (80.4 mg g^{-1} for $Ti_3C_2T_x$/CuHCF) in conjunction with an ultrafast removal rate of 43.3 mg g^{-1} min^{-1} with a NaCl concentration of 1000 mg L^{-1} at 1.4 V. And an excellent charge efficiency (above 90%) and cycling stability were also demonstrated.

In addition, the exploitation of CDI electrodes has been rarely conducted to capture Cl^- ions, in which most of the CDI research focused on the cation storage. Then, Lei *et al.*[113] fabricated a self-supporting CoFe-layered double hydroxide (CoFe-LDH)/$Ti_3C_2T_x$ film *via* facile vacuum filtration, as displayed in Fig. 4e, and utilized it as the Cl^- stored electrode. The high exposed adsorption sites, conductive framework, and hierarchical micro-mesoporous structure deriving from the interweaving layered CoFe-LDH with conductive $Ti_3C_2T_x$, led to the ultrahigh desalination capacity of 149.25 ± 6.17 mg g^{-1} at a current density of 50 mA g^{-1} with an optimal desalination rate of 3.86 mg g^{-1} min^{-1} at 100 mA g^{-1} under a NaCl solution concentration of 20 mM. Moreover, the hybrid CDI system, using the LDH/$Ti_3C_2T_x$ electrode as anode, exhibited low energy consumption of 0.32 ± 0.03 kW h kg^{-1}, excellent charge efficiency, and good regeneration with a capacity retention of 81.7% after 30 cycles.

In general, vacuum filtration represents a promising strategy for the preparation of freestanding films with desirable properties, providing a valuable platform for the development of high-performance CDI electrodes. However, the freestanding CDI electrodes fabricated by the vacuum filtration method have exclusively focused on carbon-based and MXene-based materials in recent years. Therefore, it is necessary to exploit versatile innovative Faradaic materials utilized for freestanding CDI electrodes *via* vacuum filtration. And the vacuum filtration method is only suitable for specific materials with a specific size and film-forming property, which severely hindered its further development.

3.3. Paste rolling and molding

Paste rolling is another robust template-free method to prepare freestanding electrodes used for CDI without supporting substrates. Typically, the pre-treated slurry is rolled into macroscopic freestanding films under external pressure (Fig. 5a). Most of the paste rolling-based process utilizes the binders to integrate each individual component, forming freestanding films. The as-fabricated freestanding electrodes have good homogeneity, excellent denseness, and controllable thickness compared to those prepared *via* the traditional manual slurry-coated method, which further significantly reduced the labor input. Until now, carbon-based materials and some other materials (*e.g.*, AC,[114] N-doped graphene,[115] porous carbon,[116] MXene,[117] and Prussian blue analogues (PBAs)[118]) have been adopted as freestanding CDI electrodes for ion uptake *via* the paste rolling method. For instance, Chen *et al.*[119] tailored a special architecture with sub-sized $Ti_3C_2T_x$ intercalated by Na^+ ions (Na^+–$Ti_3C_2T_x$-MS). Then, the freestanding films were obtained by rolling the mixed slurry of Na^+–$Ti_3C_2T_x$-MS, carbon black, and polytetrafluoroethylene (PTFE) binder with the ratio of 8.5 : 1 : 0.5, respectively. Moreover, the enlarged interlayer spacing derived from the Na^+ intercalation and suitable sub-sized particles can effectively supply the sufficient active constituent, optimize the ion diffusion path, and improve the desalination kinetics. Thus, the freestanding Na^+–$Ti_3C_2T_x$-MS film electrode exhibited a high desalination capacity of 14.8 mg g^{-1} and charge efficiency of 0.81 associated with good cycling stability in a 100 mg L^{-1} NaCl solution under a cell voltage of 1.2 V.

Furthermore, Singh *et al.*[120] proposed a vanadium hexacyanoferrate (VHCF, a PBA) electrode encapsulated with a protective conducting polymer (poly-pyrrole, doped with polystyrene sulfonate), using the coprecipitation method with subsequent cold-rolling and electrodeposition treatment, as freestanding CDI electrodes for selective ion removal towards water remediation. Specifically, a hybrid CDI cell (Fig. 5b) consisting of a VHCF electrode coated with a protective layer worked as the cathode for selective removal of divalent ions, and an oversized activated carbon isolated using an anion-exchange membrane (AEM) from the mixed stream, worked as the anode. Moreover, the protective conducting polymer, which effectively cut off the contact between the electrode and feed stream, essentially eliminated the contamination of treated solution caused by the leaching of electrode components. As a result, the VHCF electrode exhibited preferential adsorption for divalent Ca^{2+} over monovalent Na^+, along with a separation factor of 3.5 ($\beta_{Ca/Na}$, the ratio of adsorption efficiency of target ions). Simultaneously,

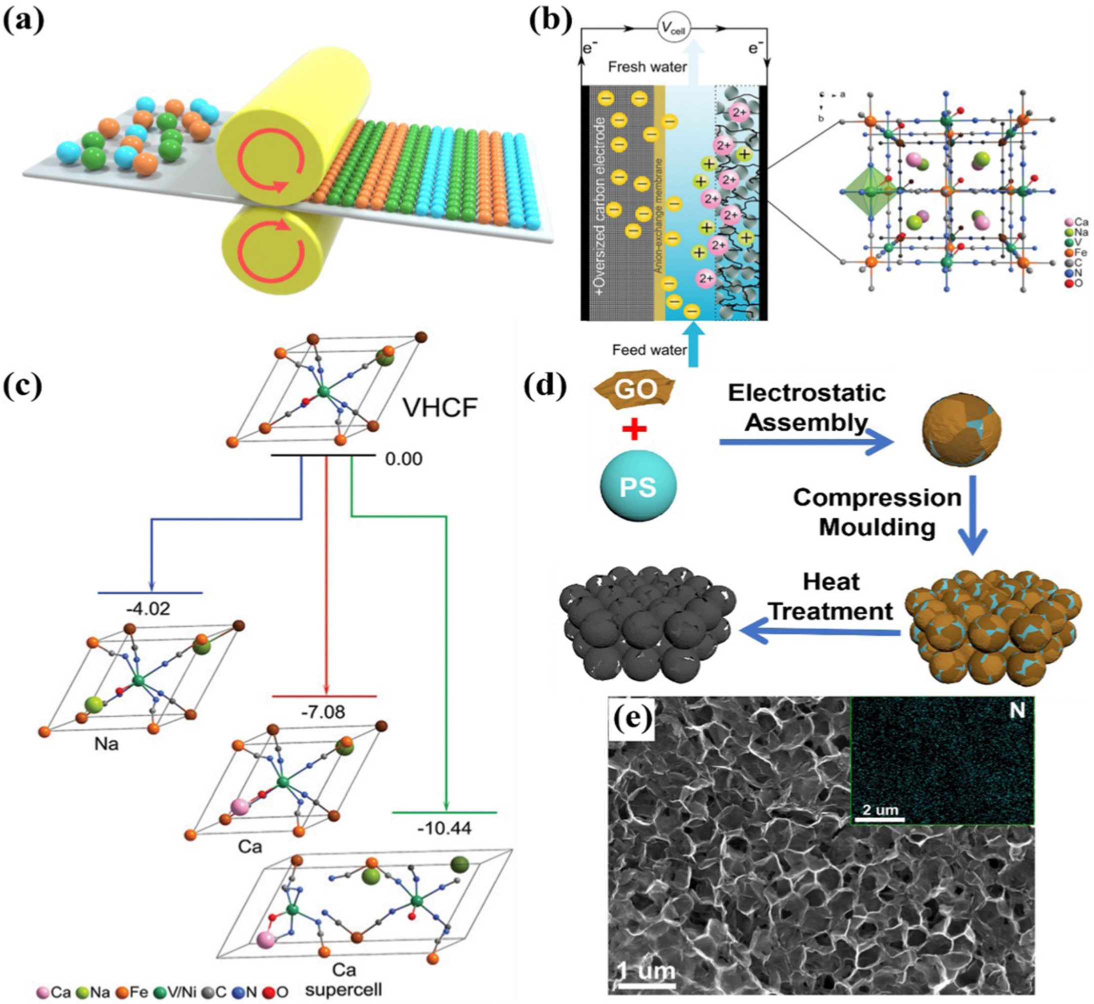

Fig. 5 (a) Schematic diagram of the paste-rolling method. (b) Schematic of the hybrid CDI cell and (c) density functional theory (DFT) calculations of the VHCF, reproduced from ref. 120 with permission from Wiley. (d) Fabrication schematic and (e) SEM image of the freestanding N-doped graphene membrane electrode, reproduced from ref. 115 with permission from Elsevier.

density functional theory (DFT) calculations also demonstrated the switched affinity toward Ca^{2+} (Fig. 5c).

More recently, Zhang *et al.*[115] used graphene oxide (GO) sheets and PS spheres as precursors to prepare the porous freestanding N-doped graphene membrane electrode (F-N-GPM) by the route of compression molding method followed by thermal treatment. Fig. 5d schematically illustrated the preparation of a freestanding F-N-GPM electrode through the compression molding method, yet without the utilization of a binder. The SEM image of the F-N-GPM electrode (Fig. 5e) implied its interconnected porous structure. The 3D interconnected network, increasing the accessible surface area, and the N doping, boosting the hydrophilicity of the electrode surface, synergistically contributed to the enhanced desalination performance. In particular, the F-N-GPM electrode delivered a desalination capacity of 21.8 mg g^{-1} with good cycling durability in a 100 mg L^{-1} NaCl solution at 1.8 V. It also exhibited a certain adsorption ability towards some other salts, including KCl, $CaCl_2$, and $MgCl_2$.

From an objective viewpoint, the freestanding CDI electrodes fabricated by the paste rolling and molding methods exhibit good homogeneity, denseness, and controllable thickness, while the unsatisfactory desalination capacity resulting from the utilization of deleterious polymeric binder catastrophically restrict their further practical application. Specifically, the effect of the polymeric additives on the electrode properties could be deemed to be correlated with the following aspects: Firstly, the polymeric binder integrates the individual components together, further forming freestanding electrodes and maintaining the structural integrity. Secondly, in general, the polymeric additives are known to be hydrophobic and electrically insulated, which could lead to the inferior ionic conductivity and electrochemical kinetics. Thirdly, the excessive use of polymeric additives can lead to decreased porosity and ion accessibility of the electrode, which can reduce the overall electrochemical performance, thereby leading to the unsatisfactory CDI performance. Therefore, these effects should be carefully considered when using polymeric additives in the fabrication process of freestanding CDI electrodes *via* paste rolling/molding methods. Moreover, the optimized procedures and the development of materials that eliminate the need for insulated binder are still urgently required.

4. Template-guided methods for the preparation of freestanding CDI electrodes

The *in situ* growth strategy, in which the target active materials are directly grown on the substrates during the preparation process, is the key factor for template-guided methods to fabricate the freestanding CDI electrode. Typically, the synthetic methods include the hydrothermal/solvothermal method, chemical bath, and thermal treatment. Additionally, the selection of appropriate substrates and target materials plays a crucial role in determining the approach for preparing freestanding electrodes. At present, the common substrates are committed to using the carbon-based and metal-based materials as assistants. Therefore, the carbon/metal-based substrates (*e.g.*, carbon cloth,[121] graphite paper,[122] Ni foam,[123] and Ti plate,[124]) with excellent conductivity and exceptional structural stability have been vigorously exploited.

4.1. Hydrothermal/solvothermal methods

The hydrothermal/solvothermal method, featured with the advantages of a one-step synthetic route, precise tunability, and modest operating conditions, is one of the most effective strategies to prepare the freestanding electrodes.[125] Generally, in a typical hydrothermal/solvothermal process (Fig. 6a), the functionalized groups (*e.g.*, oxygen-containing groups and defects) distributed on the substrates provide suitable sites for the nucleation and conformal growth of an active solid phase, thereby ensuring the uniform formation of active materials on the substrates.[126] Simultaneously, the nucleation process and crystal growth can be facilitated with the elevated temperature and pressure.[127] Therefore, the reaction conditions, such as the substrates, temperature, pH, and reactant concentration significantly affect the morphology, component, and crystal structure of the as-fabricated active materials. For instance, the pretreatment of substrates is necessary to remove the impurities

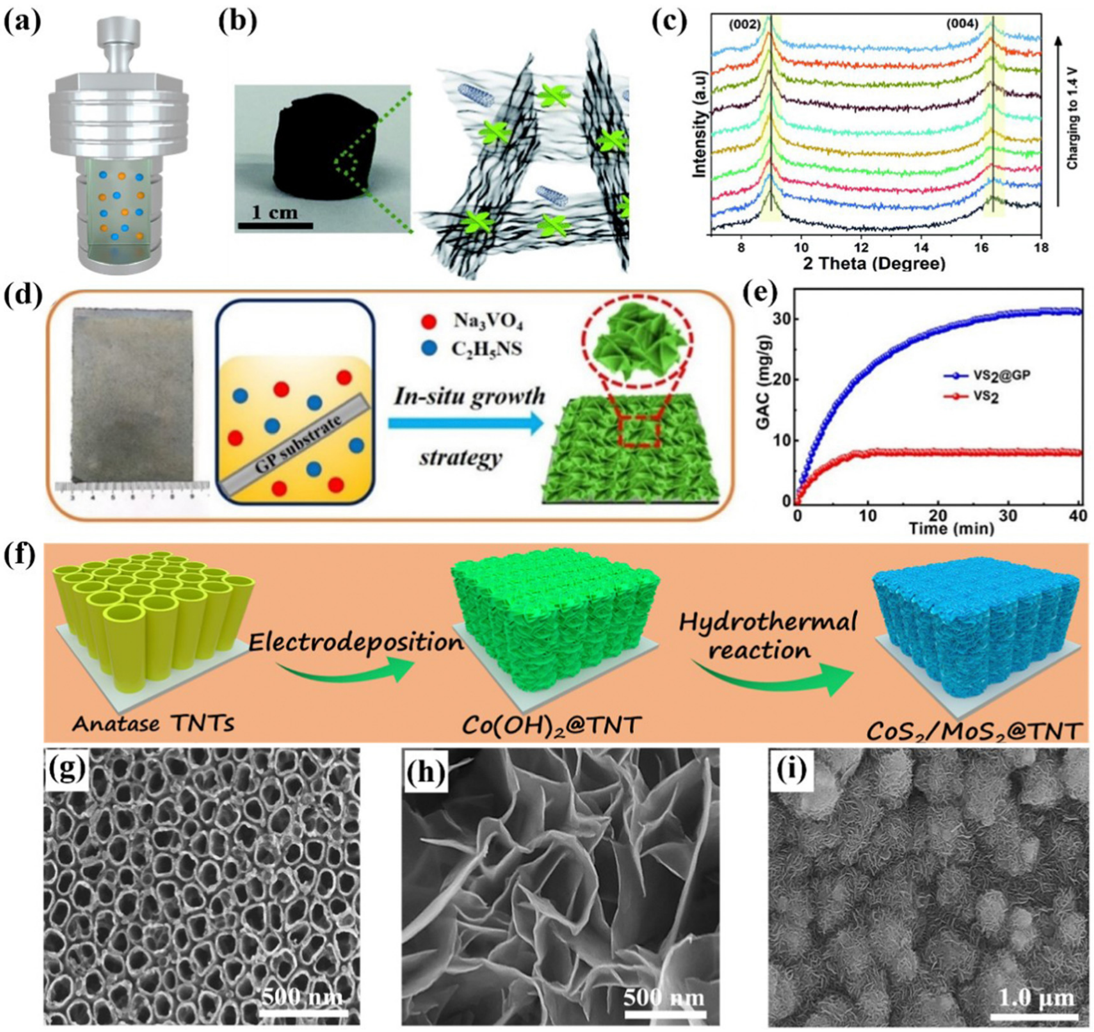

Fig. 6 (a) Schematic illustration of hydrothermal/solvothermal methods. (b) Photograph and schematic and (c) *in situ* XRD patterns during the charging step of WS_2/rGO–CNT aerogel, reproduced from ref. 131 with permission from the Royal Society of Chemistry. Schematic diagram of (d) preparation and (e) ion removal capacity of the self-supported VS_2@GP electrode, reproduced from ref. 132 with permission from the American Chemical Society. Schematic illustration of (f) the fabrication of MoS_2/CoS_2@TiO_2 nanotube hybrid electrodes, and SEM images of (h) TiO_2 nanotubes, (i) $Co(OH)_2$ skeleton, and (j) hybrid electrode, reproduced from ref. 124 with permission from Elsevier.

and increase the functionalized groups on the substrate surface. In recent years, various conductive matrices associated with versatile outperforming materials (*e.g.*, NiCoAl-mixed metal oxides,[123] Pd/NiAl-layered metal oxides,[128] $Na_3V_2(PO_4)_3$/graphene aerogels,[129] AgCl/graphene aerogels,[129] Prussian blue (PB)/graphene aerogels,[130] and WS_2/rGO-CNT aerogels[131]) have been successfully fabricated using hydrothermal/solvothermal methods.

For instance, Vafakhah *et al.*[131] prepared the freestanding WS_2/rGO-CNT aerogel as a CDI electrode through a simple solvothermal method and subsequent freeze-drying treatment. The as-fabricated freestanding aerogel and schematic structure were presented in Fig. 6b, in which the redox active WS_2 nanoflowers were embedded in the conductive interconnected rGO–CNT network without any polymeric additives/binders. In addition, the interlayer spacing of the unique WS_2 nanosheets was enlarged *via* an efficient strategy of oxygen incorporation, which could increase the ion accessibility of the electrode, further resulting in the enhanced desalination performance. At the same time, the slight shift of the characteristic peaks to lower angles with the increased voltage was confirmed by *in situ* X-ray diffraction (XRD) measurements, unveiling the expanded interlayer spacing and intercalation mechanism for the removal of Na^+ ions (Fig. 6c). The unique active redox WS_2 nanoflowers with enlarged interlayer spacing associated with the 3D conductive rGO–CNT framework synergistically improved the conductivity, facilitated the diffusion of ions, and boosted the reaction kinetics, thereby contributing to the enhanced desalination performance. As a result, the assembled hybrid CDI cell, consisting of the freestanding WS_2/rGO–CNT aerogel and rGO/CNT aerogel served as the cathode and anode, respectively, demonstrated a desalination capacity of 80 mg g^{-1} in a 3000 mg L^{-1} NaCl solution at 1 mA, an optimal removal rate of 3.90 mg g^{-1} min^{-1} at 10 mA, and a favorable lifespan.

Apart from the aforementioned metal oxides and hybrid carbon aerogel, many other freestanding CDI electrodes loaded with high-performance Faradaic materials can also be obtained by the hydrothermal/solvothermal method and directly utilized as electrodes without conductive agent, polymeric binder, and even the current collector. Our group proposed a series of related works in recent years. To date, $Co(OH)_2$ nanosheet@graphite paper (GP),[122] SnS_2 nanosheet@GP,[133] VS_2 nanosheet@GP,[132] N-doped carbon nanolayer (N-C) encapsulated titanium nitride (TiN) nanorod@carbon cloth (N-C@TiN@CC),[121] and MoS_2/CoS_2@TiO_2 nanotubes[124] were successfully fabricated as the freestanding and binder-free electrodes for CDI. For instance, we synthesized the self-supported VS_2@GP electrode consisting of VS_2 nanosheets *in situ* grown on the functionalized GP substrate *via* a facile one-step hydrothermal reaction.[132] Specifically, the preparation procedures were schematically illustrated in Fig. 6d. The conductive GP not only served as the skeleton to grow the VS_2 nanosheets, but also acted as the current collector. Benefiting from the superior hierarchical framework, binder-free synthesis process, and improved electrical conductivity, the freestanding VS_2@GP electrode demonstrated an outstanding desalination capacity of 31.19 mg g^{-1} in a 520 mg L^{-1} feed solution at 1.2 V, which was much higher than that of the powder VS_2 electrode (7.96 mg g^{-1}) fabricated using the traditional slurry-coating method (Fig. 6e). Moreover, the monolithic VS_2@GP electrode delivered a satisfactory charge efficiency (0.76) and cycle lifespan.

In addition, titanium foils, possessing the merits of exceptional electronic conductivity, excellent mechanical stability, and good chemical inertness, can be suitable scaffolds for fabricating freestanding CDI electrodes. Therefore, our group contrived a self-supported MoS_2/CoS_2@TiO_2 electrode, which consisted of Ti foil loaded with TiO_2 nanotubes encapsulated with the composite of MoS_2 and CoS_2, *via* the electrodeposition method followed by a hydrothermal process.[124] Fig. 6f shows a schematic of the *in situ* synthetic procedures. In the first step, the anatase TiO_2 nanotubes with an average diameter of about 100 nm (Fig. 6g) were fabricated by the anodic oxidation method and the subsequent annealing treatment. Subsequently, the $Co(OH)_2$ nanosheets, serving as the template of the final freestanding electrode, were deposited on the pre-obtained anatase TiO_2 nanotubes. The smooth 3D $Co(OH)_2$ nanosheets can be observed in Fig. 6h. Finally, the uniformly dispersed MoS_2/CoS_2 nanoflowers were directly grown on the TiO_2 nanotubes *via* a hydrothermal process without requiring any binders. The corresponding SEM image is shown in Fig. 6i. Furthermore, the highly open nanoflowers assembled from interconnected nanosheets, the effective combination of Faradaic materials, and the integrated self-supported electrodes synergistically ensured the effective electron transfer, improved the diffusion path of ions, and provided sufficient active sites to accommodate ions, leading to an excellent Na^+ adsorption capacity of 44.22 mg g^{-1} in a 600 mg L^{-1} feed solution at 1.2 V. Moreover, the monolithic electrodes also exhibited a satisfied cycle lifespan with a subtle decay of desalination capacity after 20 cycles.

In general, the hydrothermal/solvothermal method, based on the *in situ* growth principle, presents an effective approach for fabricating freestanding CDI electrodes, thereby eliminating the need for binders. And the reaction conditions play a critical role in determining the electrochemical properties of the resulting electrodes. However, although the hydrothermal/solvothermal method can simplify the electrode preparation process and avoid the utilization of conductive agent and polymeric binder, some intrinsic issues (*e.g.*, high-mass loading and scalable fabrication) still remain. It is also limited by the unfirm bonding between active materials and substrates and rapidly increasing manufacturing costs under thick active loaded layers.

4.2. Chemical bath deposition

Chemical bath deposition is another versatile template-assisted technique used to fabricate freestanding electrodes, processing the merits of moderate operational conditions (*e.g.*, low temperature and atmospheric pressure), low costs, and simplicity.[134,135] Typically, the chemical bath deposition process is generally conducted in a container containing the precursor solution with conductive substrates (Fig. 7a), on which target active materials are uniformly and spontaneously deposited. And the essential backbone can be readily tailored by the functionalized treatment (*e.g.*, acid etch), resulting in the generation of abundant functional

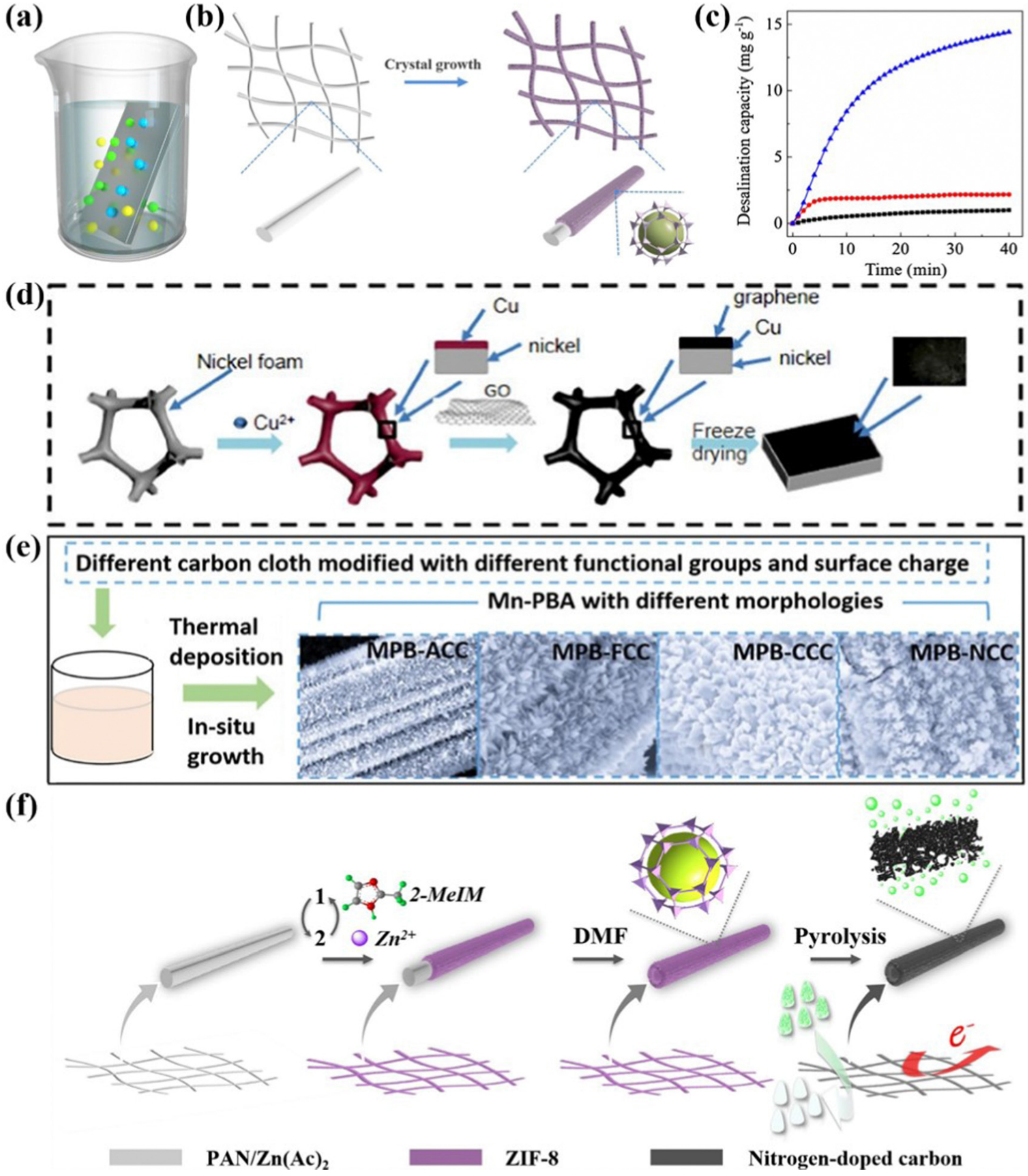

Fig. 7 (a) Schematic diagram of chemical bath deposition. (b) Scheme for the preparation of freestanding MOF electrodes and (c) comparative ion removal capacity, reproduced from ref. 141 with permission from Elsevier. Schematic illustration of the synthesis for (d) the monolithic rGO/CNF electrode, (e) Prussian blue analogues/CC electrodes, and freestanding nitrogen-doped carbon electrode, reproduced from ref. 142 and 143 with permission from Elsevier, and reproduced from ref. 144 with permission from the American Chemical Society.

groups for further anchoring the active materials. Moreover, the active material loading on the pre-treated conductive matrix can be controllable and versatile, achieved by adjusting the composition, concentration, time, and temperature.[136] In recent years, extensive efforts based on the optimized substrates, versatile active materials, and combinational post-treatments have been put forward to fabricate the monolithic CDI electrodes with enhanced deionization performance *via* the chemical bath deposition method. Specifically, SiO_2 nanoparticles/activated carbon cloth (ACC),[137] porous carbon fibers (PCF),[138] δ-MnO_2@rGO/CC,[139] and Prussian blue analogues (PBAs)/CC[140] have been successfully obtained by chemical bath deposition-based methods.

For instance, an exemplified freestanding CDI electrode through *in situ* anchoring the metal–organic framework (MOF) nanocrystals on the functionalized carbon cloth skeleton was prepared *via* the route of one-pot chemical bath deposition (Fig. 7b).[141] The monolithic electrode fabricated through the above binder-free procedure not only boosted the electrical conductivity, but also ensured sufficient accessible surface areas to accommodate target ions compared to the slurry-coated electrode. In this regard, Fig. 7c depicted the obviously enhanced desalination capacity of the freestanding nanopatterned MOF electrode (14.4 mg g^{-1}) compared to that of the coated one (2.2 mg g^{-1}) in a NaCl solution (5 mM) at 1.2 V. Moreover, the monolithic electrode demonstrated a maximum capacity of 21.3 mg g^{-1} in a 40 mM NaCl solution at 1.2 V, and an outstanding cycle lifespan with little capacity fading after 30 cycles.

As aforementioned, modulating the conductive matrix, such as incorporating binary substrates and modifying surface charge, is another promising strategy to fabricate the integrated CDI electrodes with boosted desalination performance. Li *et al.*[142] introduced an innovative binary Cu–Ni foam (CNF) serving as the backbone and current collector to couple with reduced graphene oxide (rGO) using a route of two-step chemical bath deposition followed by freeze drying. The synthetic procedures displayed in Fig. 7d implied that the monolithic rGO/CNF electrode was fabricated by *in situ* growing rGO onto the binary CNF substrate without the assistance of polymeric binders. In this work, the authors were committed to generating Ni foam loaded with different Cu contents by adjusting the substitution time and then modulating the structure and morphology of the integrated rGO/CNF electrode, thereby featuring it with a porous network and more accessible surface area. As a result, the optimal rGO/CNF electrode contributed to the increased surface areas and facilitated ion transport, thereby leading to delivery of an excellent deionization performance with a desalination capacity of 84.6 mg g^{-1} (2.23 times higher than that of rGO with the single Ni substrate), a satisfactory removal rate of 4.88 mg g^{-1} min^{-1}, and an acceptable long-term stability (over 91% capacity retention after 20 cycles) in a 250 mg L^{-1} NaCl solution at 1.2 V. In addition, Zhang *et al.*[144] synthesized manganese (Mn)-based Prussian blue analogues (MPBs) loaded on various tailored substrates (*e.g.*, the acid-treated carbon cloth (ACC), F-doped carbon cloth (FCC), chitosan-coated carbon cloth (CCC), and N-doped carbon cloth (NCC)) to investigate the effects of different functional groups and surface charge on the carbon cloth towards desalination performance. Specifically, the different monolithic MPB/CC electrodes were fabricated using a facile chemical bath deposition method, and directly utilized as the CDI electrode in a hybrid CDI system (Fig. 7e). Integrating the advantages of the modified carbon cloth and nanostructured MPBs, the freestanding MPBs/FCC electrode demonstrated the highest desalination capacity of 10.92 mg g^{-1}, and the highest charge efficiency (82.28%) in conjunction with the lowest energy consumption (0.45 kW h m^{-3}).

Furthermore, leveraging the post-treatment coupled with the chemical bath deposition process is also an effective strategy to obtain the freestanding CDI electrodes. Xu *et al.*[143] elaborately developed monolithic tubular N-doped carbon tubes (NCTs) derived from a MOF *via* chemical bath deposition followed by unique etch and pyrolysis treatment. The fabrication procedures are presented in more detail in Fig. 7f. The as-fabricated freestanding NCTs were attached to a current collector directly serving as the CDI electrode without adding any conducive agents and deleterious binders. The unique tubular architecture, binder-free electrode configuration, and abundant nitrogen dopants synergistically improved the diffusion path of electrons and ions, provided enough accessible surface areas, and enhanced the electrical conductivity, thereby boosting the deionization performance. Accordingly, the NCTs delivered an excellent CDI performance with a maximum desalination capacity of 56.9 mg g^{-1} in a 60 mM NaCl solution under 1.2 V with good cycling stability.

Overall, chemical bath deposition is a promising technique that offers several benefits for the fabrication of freestanding CDI electrodes, in which the active materials can be directly deposited onto the pre-treated matrix, forming the monolithic CDI electrode without the assistance of conductive additives and binders. However, although various integrated CDI electrodes have been proposed, the unsatisfied desalination capacity is an important factor hindering their further practical applications. Thus, exploiting versatile conductive substrates coupled with more high-performance Faradaic materials *via* the chemical bath deposition-based methods is still in high demand.

4.3. Thermal treatment

Thermal treatment is an exclusive method to fabricate the self-supported monolithic CDI electrodes, which are mostly derived from carbon cloth/wood-based materials, serving not only as the substrates, but also the active materials.[145–147] In the context of thermal treatment process (Fig. 8a), the carbon-based precursor is converted to self-supported integrated CDI electrodes, featured with versatile structures, morphologies, porosity, and doping characteristics, by the carbonization, activation, and combination process under sintering at high temperature. At present, this robust method has been applied to obtain various carbon-based monolithic electrodes, which can be categorized into carbon fiber-based (*e.g.*, carbon nanofiber aerogels[145,148–150] and variable activated carbon cloth[151–154]) and wood-based (converted from various wood such as beech wood,[155] basswood,[147] and balsa[146]) materials.

In an exemplified sample, Ahn *et al.*[156] developed a nitrogen-incorporated porous activated carbon cloth (N-ACC), which was directly engaged as the integrated binder-free redox-mediated deionization (Redox-DI) electrodes *via* a judicious thermal deposition method. Specifically, the N-ACC with high catalytic activity groups (Fig. 8b) was obtained by a simple heat treatment utilizing urea as the nitrogen source. Moreover, the assembled Redox-DI cell (Fig. 8c) consisting of the as-fabricated monolithic N-ACC electrodes serving as both the cathode and anode and the $Na_3Fe(CN)_6/Na_4Fe(CN)_6$ solution as the redox intermediates was proposed. On account of the enhanced electrocatalytic activity, improved reaction kinetics, and decreased transfer resistance of redox couple reactions derived from N doping, the binder-free N-ACC electrodes delivered an ultrahigh desalination capacity of 69.1 mg g^{-1}, and a remarkable charge efficiency of 95.3% in conjunction with an energy consumption of 122.0 kJ mol^{-1} with a stream brine solution of 10 mM.

Moreover, as for the wood converted route, He *et al.*[146] synthesized binder-free wood converted porous carbon utilizing natural balsa, pine, and basswood *via* the thermal treatment subsequently activated by the chemical bath route. And the as-prepared wood converted carbon was directly attached to the

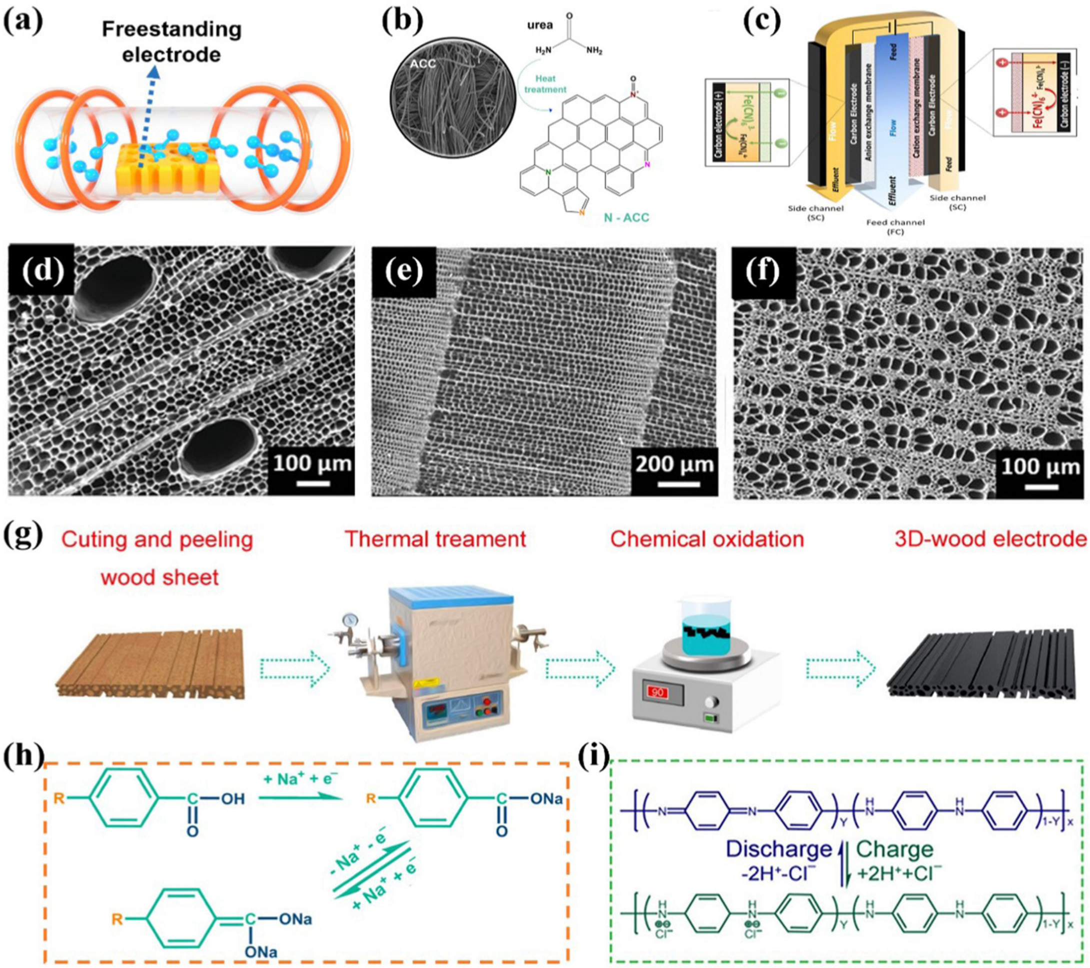

Fig. 8 (a) Schematic of the thermal treatment process. Illustration of (b) the fabrication of activated carbon cloth and (c) redox-deionization cell, reproduced from ref. 156 with permission from Elsevier. SEM images of (d) carbonized balsa, (e) carbonized pine, and (f) carbonized bass, reproduce from ref. 146 with permission from Wiley. Schematic diagrams of (g) the preparation of a 3D wood electrode and (h and i) ion uptake mechanisms, reproduced from ref. 157 with permission from the America Chemical Society.

current collector used as the freestanding CDI electrode without any binder. In addition, the surface morphology of the carbonized wood demonstrated different pore structures. Specifically, as shown in Fig. 8d, the carbonized balsa exhibited two tunnel sizes of dominated small channels associated with less large channels. The SEM image of carbonized pine (Fig. 8e) manifested its noticeable uniform tunnel structure. Furthermore, the carbonized bass exhibited a dispersed porous structure with varying channel sizes, attributed to the obstruction caused by the carbonized organic tissue (Fig. 8f). The activated balsa electrode integrated the advantages of extensive surface area, enhanced electrical properties, and improved hydrophilicity, enabling the superior deionization performance. As expected, the binder-free balsa electrode displayed a salt removal capacity of 12.45 mg g^{-1} in a 500 mg L^{-1} NaCl solution at 1.2 V, which was higher than most pure wood converted carbon electrodes. Meanwhile, the activated balsa electrode exhibited an extraordinary adsorption ability for heavy metal toxic ions of Pb^{2+} and Cr^{3+} in 100 mg L^{-1} $PbCl_2$ and 50 mg L^{-1} $CrCl_3$, respectively, under 1.2 V.

Additionally, Wei *et al.*[157] designed an all-wood-based battery deionization cell designated as battery deionization (BDI) comprising a self-supported wood electrode in conjunction with a freestanding polyaniline (PANI)-modified wood electrode serving as the cathode and anode, respectively. As shown in Fig. 8g, the 3D wood electrode was fabricated by thermal treatment followed by functionalization with redox-active sites *via* a chemical oxidation process, associated with the waste wood as raw materials. Specifically, the hemicellulose and cellulose components in native wood were efficiently converted into carbon materials under thermal treatment. Simultaneously, the lignin component underwent slight structural modifications, resulting in the loss of certain functional groups while preserving its fundamental structure, which plays a crucial role in ion capture for the final electrode. Meanwhile, the PANI, featured with the variability among three discrete oxidation states, was electrodeposited on the thermal-treated wood to obtain the PANI-modified wood electrode. Moreover, the authors proposed the underlying ion-uptake mechanisms (Fig. 8h and i), in which the cations were captured by hydrophilic –OH and reactive –C═O combined with protonated imine nitrogen atoms for anion removal under electrochemical redox conditions. Integrating the as-prepared 3D wood electrode with abundant redox-active sites, reinforced hydrophilicity, and modulated porosity with the PANI-modified wood electrode, the assembled cell exhibited an outperformed total ion (*i.e.*, Na^+, Mg^{2+}, and Cl^-) deionization capacity of 164 mg g^{-1} in real seawater.

In summary, the thermal treatment is a robust approach for fabricating monolithic carbon-based CDI electrodes, and the rational modulation of organic components in wood precursor is a crucial factor in determining the properties (*e.g.*, porosity, hydrophilicity, and morphology) of the final electrodes. However, from an objective standpoint, the inferior desalination capacity resulting from the inherent disadvantages of carbon-based CDI, such as deleterious co-ion expulsion and intolerance at high salinity, severely limits their practical application. In addition, the intensive studies outlined above mainly focused on exploring the hydrophilicity, porosity, and activation types of monolithic thermal-treated carbon-based CDI electrodes towards ion-selective adsorption and ion sieving. Thus, the standardized metrics increasingly need to be delineated for quantification and comparison of various CDI systems for selective ion removal.

5. Other methods for the synthesis of freestanding CDI electrodes

In addition to the aforementioned template-free and template-assisted methods, some other less-common strategies (*e.g.*, the sol–gel method,[158–160] electrodeposition,[161–164] chemical vapor deposition,[165] atomic layer deposition,[166] and 3D printing technique,[167]) in the CDI community have been adopted to fabricate the freestanding electrodes.

The sol–gel method, featuring low cost, moderate processing temperature and simplicity, is a facile strategy to prepare versatile gels with various physicochemical properties,[168–170] indicating its practical prospects in the CDI community. For example, Ding *et al.*[159] proposed a freestanding Mg^{2+}-MXene aerogel *via* the sol–gel method and subsequent freeze-drying treatment without incorporating any external polymeric binders, serving as the CDI electrodes. Moreover, the authors demonstrated an accessible strategy for the scalable fabrication of large-area Mg^{2+}-MXene aerogels using PS spheres as substrates (Fig. 9a). Specifically, the uniform crumple-textured MXene (CT-MXene) platform with the oxygen-plasma treated PS as the backbone was first obtained through a drop-cast method combined with modulation by the doctor blade method. And the freestanding Mg^{2+}-MXene aerogels derived from the freeze-dried Mg^{2+}-MXene hydrogel were stripped from the matrix. Thus, the final freestanding electrode was devoid of any residual polymeric additives or binders. Furthermore, the SEM images demonstrated the similarly oriented mesopores of binder-free Mg^{2+}-MXene aerogels and CT-MXene platforms (Fig. 9a). Owing to the boosted electrical conductivity, enlarged surface area, and high robustness in water, the Mg^{2+}-MXene aerogels delivered an outstanding desalination performance (capacity: 33.3 mg g^{-1}; desalination rate: 1.1 mg g^{-1} min^{-1}) with a satisfactory long-term stability (over 30 cycles).

In addition, chemical vapor deposition has received considerable attention for fabricating electrodes in the energy storage field.[171–173] For instance, Song *et al.*[165] prepared a freestanding CNT film as binder-free CDI electrodes *via* floating-catalyst chemical vapor deposition (FCCVD). In the context of the fabrication process, the CNT aerogel, derived from the decomposition of polymeric precursors, was firstly obtained under high temperature. And then the CNT gel was transferred downward *via* the hydrogen gas, thereby transformed into a CNT film at the bottom of the chamber (Fig. 9b). It is noteworthy that, despite the utilization of pyrrole as a precursor, the high-temperature pyrolysis process led to the complete decomposition and transformation of pyrrole into freestanding CNT films, precluding any residual polymeric additives in the final electrode. Furthermore, Fig. 9c shows that the binder-free CNT film had a freestanding and flexible structure. As a result, the obtained binder-free CNT film with a large specific surface area of 198 m^2 g^{-1} delivered a desalination performance of 11.39 mg g^{-1}.

Electrodeposition is another accessible method to fabricate freestanding electrodes, in which the target materials are directly deposited onto the working electrodes (conductive substrates) under an external electric field,[174] subsequently forming the integrated CDI electrodes. Thus, there is no need for the external polymeric additives or binders to integrate the individual components together. An exemplified binder-free film electrode *via* coupling the layered MXene and conductive CNT on the conductive graphite paper was prepared by the electrophoretic deposition (EPD) method.[161] Fig. 9d schematically displayed the process of EPD and the as-fabricated self-supported film electrodes with a dense and uniform structure. Moreover, the restrained self-stacking of MXene, modulated charge transfer path, improved ion diffusion kinetics, and more spacious ion-insertion sites derived from the synergistic effects of conductive CNT and the binder-free BED method were proposed to enhance the desalination performance. Consequently, the integrated MXene/CNT film electrode attained an outstanding desalination performance with a desalination capacity of 34.5 mg g^{-1}, a removal rate of 3 mg g^{-1} min^{-1}, and a low energy consumption of 0.26 kW h kg^{-1} associated with excellent long-term stability (retention of 89% after 40 cycles) in a 500 mg L^{-1} feed stream at 1.2 V, which was much higher than that of the conventional slurry-coated electrode (18.7 mg g^{-1}).

Additionally, the 3D printing method has attracted enormous attention as a novel technique for rapid prototyping in many applications.[175,176] Recently, Vafakhah *et al.*[167] contrived a freestanding integrated nitrogen-doped GO/CNT electrode *via* 3D printing technology (Fig. 9e), in which there was no need for any polymeric additives. As a result, the monolithic 3D printed electrodes delivered an ultrahigh desalination of 75 mg g^{-1} at 100 mA g^{-1}, a low energy consumption of 0.331 W h g^{-1} with a removal capacity of 60 mg g^{-1}, as well as excellent cycling lifespan (50 cycles).

To conclude, although versatile less-common methods have been exploited to fabricate freestanding electrodes in the CDI

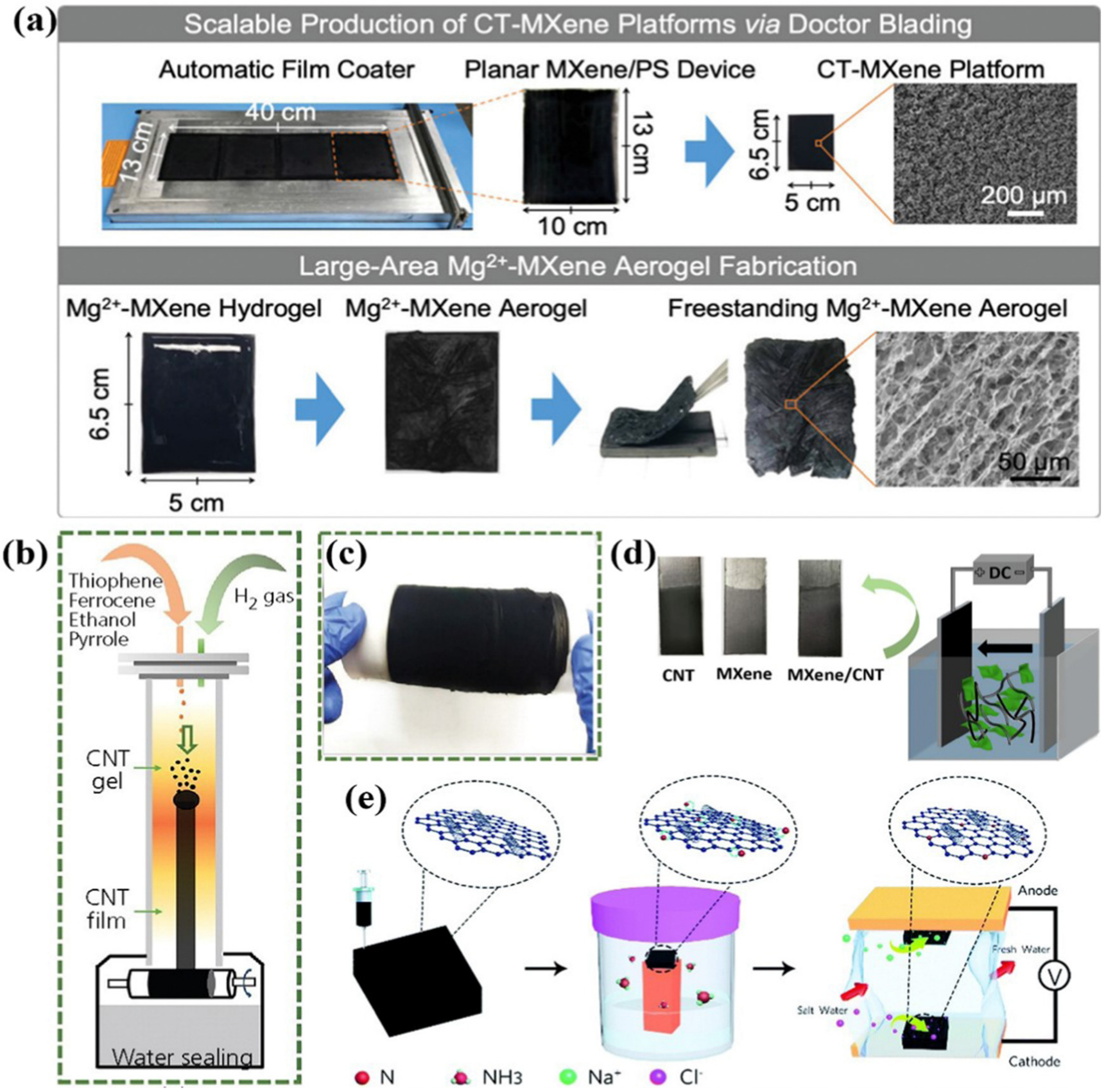

Fig. 9 (a) Illustration of the scalable fabrication of large-area Mg^{2+}-MXene aerogels,[159] reproduced with permission from Wiley. (b) Schematic diagram of the preparation of CNT film and (c) a digital photograph of the as-fabricated CNT film, reproduced from ref. 165 with permission from ICE publishing. (d) Digital photographs of the as-prepared freestanding electrodes and scheme of the electrophoretic deposition process, reproduced from ref. 161 with permission from Elsevier. (e) Schematic illustration of the fabrication of the N-doped GO/CNTs electrode and CDI cell, reproduced from ref. 167 with permission from the Royal of Society of Chemistry.

field, the rational selection of materials, demand of polymeric additives, and modulation of components should also be taken into consideration for novel fabrication strategies. Moreover, there is a growing demand to excavate and replenish novel techniques for the preparation of integrated CDI electrodes combined with an outstanding deionization performance.

6. Summary and outlook

Having burgeoned as a promising alternative towards brackish water remediation, CDI has received considerable attention in recent years. In all cases, the electrodes play a crucial role in high-performance and efficient CDI. Compared with conventional slurry-coated electrodes, freestanding electrodes integrate simplified fabrication procedures, enhanced electrical conductivity, and improved cycle lifespan, contributing to boost the deionization performance. In this review, we put forth a comprehensive overview of recent advances in the fabrication strategies of freestanding electrodes and related performance metrics (*e.g.*, ion removal capacity, ion removal rate, charge efficiency, and energy consumption) for CDI. Specifically, the preparation methods of freestanding electrodes (mostly binder-free) are conceptually categorized into template-free methods, template-guided methods, and some other less-common methods. Template-free methods involving electrospinning, vacuum filtration, and paste-rolling methods can synthesize the freestanding electrodes without the prepared substrates. And template-guided methods, depending largely on *in situ* growth onto a conductive matrix (*e.g.*, Ni foam, Ti plate, graphite paper, and carbon cloth), mainly include hydrothermal/solvothermal methods, chemical bath deposition, and thermal treatment. Moreover, other less-common methods, such as 3D printing, can also be used to fabricate freestanding electrodes. Table 1 summarizes recent freestanding electrodes with their corresponding synthetic methods and deionization performance. Furthermore, Table 2 provides a summary of the typical values for various properties of electrodes fabricated using the aforementioned methods.

Although substantial deployment of freestanding electrodes has been achieved, the field is not yet mature enough to meet the requirements for practical applications. And several major challenges still remain in the further development of freestanding electrodes. (i) Fabrication methods. Although versatile strategies have been adopted to prepare the freestanding CDI electrodes, each method has its own limitations. In terms of the main methods (*e.g.*, electrospinning, vacuum filtration, and hydro/solvothermal) currently available, for example, freestanding electrodes constructed by the electrospinning technique depend largely on the composition of precursors, and subsequent thermal treatment is usually needed. Moreover, the hydro/solvothermal method still suffers from the challenges of high-mass loading, cycling durability, and scalable fabrication of electrodes. Besides, the related CDI performance is still unsatisfactory for practical applications. So, it is imperative to exploit tailored methods and routes of freestanding electrodes towards high-performance CDI. In addition, the techno-economic feasibility, environmental friendliness, and large-scale fabrication should also be considered. Notably, rational combination of different strategies and exploitation of innovative techniques, such as 3D printing, can possibly be an effective way to combat the aforementioned issues.

(ii) Advanced materials for freestanding electrodes. Carbon-based and Faradaic materials mostly possess intrinsic disadvantages in terms of moderate removal capacity caused by the deleterious co-ion expulsion and inferior structural stability derived from the unaccommodated volume change, respectively. Hence, combining stable and conductive carbon-based materials with high-capacity Faradaic materials has been deemed as an efficient way to prepare freestanding electrodes with enhanced deionization performances in recent years. However, a major obstacle of high manufacturing costs of some carbon-based materials (*e.g.*, graphene and CNTs) and unsatisfactory ion removal capacity still remains, thus hindering their further practical application. Therefore, the underlying correlation from the inherent properties of electrodes to deionization performance, novel materials, and the exploitation of instructive strategies (*e.g.*, rational modulation of component ratio, advanced structural design, and judicious phase engineering) should be replenished to fabricate the freestanding electrodes with a combined CDI performance, thereby addressing these challenges. Meanwhile, in terms of the rare exploitation of Cl^- stored materials, more intensive advanced materials for freestanding electrodes toward Cl^- removal need to be explored to alleviate the issue of differentiated adsorption kinetics between Na^+ and Cl^-, thus enabling further optimization of the CDI performance.

(iii) Regarding the CDI process, the electrical conductivity, hydrophilicity, and texture properties are crucial factors in determining the deionization performance of all CDI electrodes including the freestanding/binder-free electrodes. Therefore, it is crucial to rationally modulate the relevant properties of freestanding/binder-free electrodes to enhance their deionization performance. Furthermore, given the fundamental structure of freestanding/binder-free electrodes, which consists of interconnected conductive substrates and active materials, and the relevant properties for optimal performance, a straightforward design guideline can be proposed. Firstly, the selection of appropriate conductive substrates and materials that ensure good connectivity, good electrical conductivity, and intimate attachment is critical. Secondly, the rational modulation of microstructure/morphology of the active materials to obtain the superior texture and diffusion kinetic properties, which could ensure good connectivity among each individual component, thereby improving the overall conductivity. Finally, the rational reconfiguration of the surface properties (*e.g.*, chemical activation) could play a critical role in decreasing the interface resistance between the electrode and electrolyte, thereby increasing the accessible surface area for ions. In summary, from an objective standpoint, a rational design guideline is of great significance for the fabrication of high-performance freestanding/binder-free CDI electrodes. However, the rational tradeoffs among relevant components, structure, and properties remain challenges due to the various materials and methods. Therefore, there is still much work to be done in this field.

(iv) Tailored applications. Until now, the advanced CDI materials show great promise for tailored applications ranging from the water desalination to ion sieving and heavy metal removal.[2,22,177,178] However, the current research towards freestanding CDI electrodes mainly focuses on desalination, in which only rare studies on selective ion and heavy metal removal have been proposed. Thus, for the further development of freestanding electrodes, the exploitation towards tunable applications outlined above is definitely required, ensuring its competitive advantages compared with conventional materials and methods.

Table 2 Typical values for various properties of electrodes fabricated using the aforementioned methods

Methods	Mass loading (mg)	Thickness	Porosity (surface area, $m^2 g^{-1}$)	Permeability
Slurry-cast	∼10–200	∼200–500 μm	∼100–1000	Average
Electrospinning	∼50–200	∼200–500 μm	∼400–1300	Good
Vacuum filtration	∼30–150	∼20–500 μm	∼100–1000	Good
Paste-rolling and molding	∼40–120	∼200–500 μm	∼100–800	Average
Hydrothermal/solvothermal	∼20–150	∼10–100 nm	∼100–1000	Good
Chemical bath deposition	∼20–150	∼10–100 nm	∼100–1000	Good
Thermal treatment	∼40–200	—	∼400–2000	Good

In summary, the versatile freestanding CDI electrodes fabricated by the recent advanced methods show great promise in the field of CDI community. Although challenges, including tunable synthetic methods, advanced materials, and tailored applications, still remain, it can be foreseen that the well-crafted freestanding CDI electrodes will provide a promising platform for the effective water remediation applications, therefore leading to a sustainable solution towards global water shortages.

Conflicts of interest

There are no conflicts to declare.

Acknowledgements

The authors gratefully acknowledge the financial supports from the Shenzhen Science and Technology Program (No. JCYJ20190809161407424), the National Natural Science Foundation of China (No. 21901131, No. 22075237), the University Student Innovation Foundation of IMU (No. 202210126034), the Young Talents of Science and Technology in Universities of Inner Mongolia Autonomous Region (No. NJYT23032), the Natural Science Foundation of Fujian Province of China (No. 2020J01007), and the Fundamental Research Funds for the Central Universities of China (No. 20720210029).

References

1 M. Rodell, J. S. Famiglietti, D. N. Wiese, J. T. Reager, H. K. Beaudoing, F. W. Landerer and M. H. Lo, *Nature*, 2018, **557**, 651–659.

2 P. Srimuk, X. Su, J. Yoon, D. Aurbach and V. Presser, *Nat. Rev. Mater.*, 2020, **5**, 517–538.

3 H. Wang, X. Mi, Y. Li and S. Zhan, *Adv. Mater.*, 2020, **32**, 1806843.

4 M. A. Shannon, P. W. Bohn, M. Elimelech, J. G. Georgiadis, B. J. Mariñas and A. M. Mayes, *Nature*, 2008, **452**, 301–310.

5 F. A. AlMarzooqi, A. A. A. Ghaferi, I. Saadat and N. Hilal, *Desalination*, 2014, **342**, 3–15.

6 S. F. Anis, R. Hashaikeh and N. Hilal, *Desalination*, 2019, **468**, 114077.

7 H.-R. Chae, J. Lee, C.-H. Lee, I.-C. Kim and P.-K. Park, *J. Membr. Sci.*, 2015, **483**, 128–135.

8 H. Strathmann, *Desalination*, 2010, **264**, 268–288.

9 J. J. Urban, *Joule*, 2017, **1**, 665–688.

10 C. Klaysom, T. Y. Cath, T. Depuydt and I. F. J. Vankelecom, *Chem. Soc. Rev.*, 2013, **42**, 6959–6989.

11 M. Sadrzadeh and T. Mohammadi, *Desalination*, 2008, **221**, 440–447.

12 T. Liu, J. Serrano, J. Elliott, X. Yang, W. Cathcart, Z. Wang, Z. He and G. Liu, *Sci. Adv.*, 2020, **6**, eaaz0906.

13 Y. Liu, K. Wang, X. Xu, K. Eid, A. M. Abdullah, L. Pan and Y. Yamauchi, *ACS Nano*, 2021, **15**, 13924–13942.

14 M. E. Suss, S. Porada, X. Sun, P. M. Biesheuvel, J. Yoon and V. Presser, *Energy Environ. Sci.*, 2015, **8**, 2296–2319.

15 R. Wang, K. Sun, Y. Zhang, C. Qian and W. Bao, *J. Mater. Chem. A*, 2022, **10**, 6414–6441.

16 X. Xu, H. Tan, Z. Wang, C. Wang, L. Pan, Y. V. Kaneti, T. Yang and Y. Yamauchi, *Environ. Sci.: Nano*, 2019, **6**, 981–989.

17 B. Zhang, A. Boretti and S. Castelletto, *Chem. Eng. J.*, 2022, **435**, 134959.

18 C. Zhang, J. Ma, L. Wu, J. Sun, L. Wang, T. Li and T. D. Waite, *Environ. Sci. Technol.*, 2021, **55**, 4243–4267.

19 H. Wang, D. Zhang, T. Yan, X. Wen, J. Zhang, L. Shi and Q. Zhong, *J. Mater. Chem. A*, 2013, **1**, 11778–11789.

20 X. Wen, D. Zhang, T. Yan, J. Zhang and L. Shi, *J. Mater. Chem. A*, 2013, **1**, 12334–12344.

21 H. Wang, T. Yan, J. Shen, J. Zhang, L. Shi and D. Zhang, *Environ. Sci. Nano*, 2019, **7**, 317–326.

22 Q. Li, Y. Zheng, D. Xiao, T. Or, R. Gao, Z. Li, M. Feng, L. Shui, G. Zhou, X. Wang and Z. Chen, *Adv. Sci.*, 2020, **7**, 2002213.

23 F. Yu, L. Wang, Y. Wang, X. Shen, Y. Cheng and J. Ma, *J. Mater. Chem. A*, 2019, **7**, 15999–16027.

24 L. Chang, Y. Fei and Y. H. Hu, *J. Mater. Chem. A*, 2020, **9**, 1429–1455.

25 P. Ratajczak, M. E. Suss, F. Kaasik and F. Béguin, *Energy Storage Mater.*, 2018, **16**, 126–145.

26 X. Zang, Y. Xue, W. Ni, C. Li, L. Hu, A. Zhang, Z. Yang and Y.-M. Yan, *ACS Appl. Mater. Interfaces*, 2020, **12**, 2180–2190.

27 P. Liu, H. Wang, T. Yan, J. Zhang, L. Shi and D. Zhang, *J. Mater. Chem. A*, 2016, **4**, 5303–5313.

28 H. Duan, T. Yan, Z. An, J. Zhang, L. Shi and D. Zhang, *RSC Adv.*, 2017, **7**, 39372–39382.

29 H. Duan, T. Yan, G. Chen, J. Zhang, L. Shi and D. Zhang, *Chem. Commun.*, 2017, **53**, 7465–7468.

30 P. Liu, T. Yan, L. Shi, H. S. Park, X. Chen, Z. Zhao and D. Zhang, *J. Mater. Chem. A*, 2017, **5**, 13907–13943.

31 A. Omosebi, X. Gao, J. Landon and K. Liu, *ACS Appl. Mater. Interfaces*, 2014, **6**, 12640–12649.

32 C. Prehal, C. Koczwara, H. Amenitsch, V. Presser and O. Paris, *Nat. Commun.*, 2018, **9**, 4145.

33 F. Chen, Y. Huang, L. Guo, L. Sun, Y. Wang and H. Y. Yang, *Energy Environ. Sci.*, 2017, **10**, 2081–2089.

34 S. Choi, B. Chang, S. Kim, J. Lee, J. Yoon and J. W. Choi, *Adv. Funct. Mater.*, 2018, **28**, 1802665.

35 Y. Li, Z. Ding, J. Li, J. Li, T. Lu and L. Pan, *Desalination*, 2019, **469**, 114098.

36 G. Wang, T. Yan, J. Zhang, L. Shi and D. Zhang, *Environ. Sci. Technol.*, 2020, **54**, 8411–8419.

37 M. Mao, T. Yan, G. Chen, J. Zhang, L. Shi and D. Zhang, *Environ. Sci. Technol.*, 2021, **55**, 730–737.

38 M. Mao, T. Yan, J. Shen, J. Zhang and D. Zhang, *Environ. Sci. Technol.*, 2021, **55**, 3333–3340.

39 M. Pasta, C. D. Wessells, Y. Cui and F. L. Mantia, *Nano Lett.*, 2012, **12**, 839–843.

40 J. Lee, S. Kim, C. Kim and J. Yoon, *Energy Environ. Sci.*, 2014, **7**, 3683–3689.

41 K. C. Smith and R. Dmello, *J. Electrochem. Soc.*, 2016, **163**, A530–A539.

42 H. Wang, D. Wei, H. Gang, Y. He, H. Deng, L. Hou, Y. Shi, S. Wang, W. Yang and L. Zhang, *ACS Sustainable Chem. Eng.*, 2020, **8**, 1129–1136.

43 Y. Li, N. Chen, Z. Li, H. Shao, X. Sun, F. Liu, X. Liu, Q. Guo and L. Qu, *Adv. Mater.*, 2021, **33**, 2105853.

44 M. Liang, N. Liu, X. Zhang, Y. Xiao, J. Yang, F. Yu and J. Ma, *Adv. Funct. Mater.*, 2022, **32**, 2209714.

45 Z. U. Khan, T. Yan, J. Han, L. Shi and D. Zhang, *Environ. Sci.: Nano*, 2019, **6**, 3442–3453.

46 L. Hu, R. Gao, A. Zhang, R. Yang, X. Zang, S. Wang, S. Yao, Z. Yang, H. Hao and Y.-M. Yan, *Nano Energy*, 2020, **74**, 104891.

47 L. Huang, T. Yan, A. E. D. Mahmoud, S. Li, J. Zhang, L. Shi and D. Zhang, *Environ. Sci.: Nano*, 2021, **8**, 950–959.

48 G. Wang, T. Yan, J. Shen, J. Zhang and D. Zhang, *Environ. Sci. Technol.*, 2021, **55**, 11979–11986.

49 Q. Li, X. Xu, J. Guo, J. P. Hill, H. Xu, L. Xiang, C. Li, Y. Yamauchi and Y. Mai, *Angew. Chem., Int. Ed.*, 2021, **60**, 26528–26534.

50 W. Peng, W. Wang, G. Han, Y. Huang and Y. Zhang, *Desalination*, 2020, **473**, 114191.

51 S. Tian, X. Zhang and Z. Zhang, *Chem. Eng. J.*, 2021, **409**, 128200.

52 J. Han, T. Yan, J. Shen, L. Shi, J. Zhang and D. Zhang, *Environ. Sci. Technol.*, 2019, **53**, 12668–12676.

53 M. Mao, T. Yan, J. Shen, J. Zhang and D. Zhang, *Environ. Sci. Technol.*, 2021, **55**, 7665–7673.

54 J. Guo, Y. Wang, Y. Cai, H. Zhang, Y. Li and D. Liu, *Desalination*, 2022, **528**, 115622.

55 H. Wang, T. Yan, P. Liu, G. Chen, L. Shi, J. Zhang, Q. Zhong and D. Zhang, *J. Mater. Chem. A*, 2016, **4**, 4908–4919.

56 M. H. Ryou, J. Kim, I. Lee, S. Kim, Y. K. Jeong, S. Hong, J. H. Ryu, T. S. Kim, J. K. Park, H. Lee and J. W. Choi, *Adv. Mater.*, 2013, **25**, 1571–1576.

57 A. Shrivastava and K. C. Smith, *J. Electrochem. Soc.*, 2018, **165**, A1777–A1787.

58 E. R. Reale, A. Shrivastava and K. C. Smith, *Water Res.*, 2019, **165**, 114995.

59 E. R. Reale, L. Regenwetter, A. Agrawal, B. Dardón, N. Dicola, S. Sanagala and K. C. Smith, *Water Res.: X*, 2021, **13**, 100116.

60 T. Jin, Q. Han and L. Jiao, *Adv. Mater.*, 2020, **32**, 1806304.

61 G. F. Chen, T. Y. Ma, Z. Q. Liu, N. Li, Y. Z. Su, K. Davey and S. Z. Qiao, *Adv. Funct. Mater.*, 2016, **26**, 3314–3323.

62 H. Sun, Z. Yan, F. Liu, W. Xu, F. Cheng and J. Chen, *Adv. Mater.*, 2020, **32**, 1806326.

63 F. Yu, Z. Yang, Y. Cheng, S. Xing, Y. Wang and J. Ma, *Sep. Purif. Technol.*, 2021, **281**, 119870.

64 B. W. Byles, D. A. Cullen, K. L. More and E. Pomerantseva, *Nano Energy*, 2018, **44**, 476–488.

65 M. Li and H. G. Park, *ACS Appl. Mater. Interfaces*, 2018, **10**, 2442–2450.

66 T. Kim and J. Yoon, *RSC Adv.*, 2014, **5**, 1456–1461.

67 S. Porada, L. Borchardt, M. Oschatz, M. Bryjak, J. S. Atchison, K. J. Keesman, S. Kaskel, P. M. Biesheuvel and V. Presser, *Energy Environ. Sci.*, 2013, **6**, 3700–3712.

68 Z. Liu, Z. Yue and H. Li, *Sep. Purif. Technol.*, 2020, **234**, 116090.

69 K. Wei, Y. Zhang, W. Han, J. Li, X. Sun, J. Shen and L. Wang, *Desalination*, 2017, **420**, 70–78.

70 B. Shapira, E. Avraham and D. Aurbach, *Electrochim. Acta*, 2016, **220**, 285–295.

71 K. Singh, S. Porada, H. D. D. Gier, P. M. Biesheuvel and L. C. P. M. D. Smet, *Desalination*, 2019, **455**, 115–134.

72 S. A. Hawks, A. Ramachandran, S. Porada, P. G. Campbell, M. E. Suss, P. M. Biesheuvel, J. G. Santiago and M. Stadermann, *Water Res.*, 2018, **152**, 126–137.

73 Y. Qu, P. G. Campbell, L. Gu, J. M. Knipe, E. Dzenitis, J. G. Santiago and M. Stadermann, *Desalination*, 2016, **400**, 18–24.

74 E. Liu, L. Y. Lee, S. L. Ong and H. Y. Ng, *Water Res.*, 2020, **183**, 116059.

75 L. Wang, J. E. Dykstra and S. Lin, *Environ. Sci. Technol.*, 2019, **53**, 3366–3378.

76 L. Wang, G. Yang, S. Peng, J. Wang, W. Yan and S. Ramakrishna, *Energy Storage Mater.*, 2019, **25**, 443–476.

77 Z. Zhou, B. Chen, T. Fang, Y. Li, Z. Zhou, Q. Wang, J. Zhang and Y. Zhao, *Adv. Energy Mater.*, 2020, **10**, 1902023.

78 X. Li, W. Chen, Q. Qian, H. Huang, Y. Chen, Z. Wang, Q. Chen, J. Yang, J. Li and Y. W. Mai, *Adv. Energy Mater.*, 2021, **11**, 2000845.

79 X. Li, Y. Chen, H. Huang, Y.-W. Mai and L. Zhou, *Energy Storage Mater.*, 2016, **5**, 58–92.

80 Q. Ni, Y. Bai, Y. Li, L. Ling, L. Li, G. Chen, Z. Wang, H. Ren, F. Wu and C. Wu, *Small*, 2018, **14**, 1702864.

81 Q. Ni, Y. Bai, S. Guo, H. Ren, G. Chen, Z. Wang, F. Wu and C. Wu, *ACS Appl. Mater. Interfaces*, 2019, **11**, 5183–5192.

82 Q. Ni, R. Dong, Y. Bai, Z. Wang, H. Ren, S. Sean, F. Wu, H. Xu and C. Wu, *Energy Storage Mater.*, 2020, **25**, 903–911.

83 Y. Li, R. Xu, L. Qiao, Y. Li, D. Wang, D. Li, X. Liang, G. Xu, M. Gao, H. Gong, X. Zhang, H. Qiu, K. Liang, P. Chen and Y. Li, *Microporous Mesoporous Mater.*, 2022, **338**, 111889.

84 I. W. Siriwardane, N. P. W. Rathuwadu, D. Dahanayake, C. Sandaruwan, R. M. D. Silva and K. M. N. D. Silva, *Nanoscale Adv.*, 2021, **3**, 2585–2597.

85 N.-L. Liu, L.-I. Chen, S.-W. Tsai and C.-H. Hou, *Environ. Sci.: Water Res. Technol.*, 2019, **6**, 312–320.

86 M. Ding, K. K. R. Bannuru, Y. Wang, L. Guo, A. Baji and H. Y. Yang, *Adv. Mater. Technol.*, 2018, **3**, 1800135.

87 T. Hussain, Y. Wang, Z. Xiong, J. Yang, Z. Xie and J. Liu, *J. Colloid Interface Sci.*, 2018, **532**, 343–351.

88 L. Guo, J. Zhang, M. Ding, C. Gu, S. Vafakhah, W. Zhang, D.-S. Li, P. V. Y. Alvarado and H. Y. Yang, *Sep. Purif. Technol.*, 2021, **266**, 118593.

89 L. Gao, S. Liu, Q. Dong, C. Hu and J. Qiu, *Sep. Purif. Technol.*, 2022, **295**, 121280.

90 X. Gong, S. Zhang, W. Luo, N. Guo, L. Wang, D. Jia, Z. Zhao, S. Feng and L. Jia, *ACS Appl. Mater. Interfaces*, 2020, **12**, 49586–49595.

91 Y. Liu, X. Gao, L. Zhang, X. Shen, X. Du, X. Dou and X. Yuan, *Desalination*, 2020, **494**, 114665.

92 P. Nie, S. Wang, X. Shang, B. Hu, M. Huang, J. Yang and J. Liu, *Desalination*, 2021, **520**, 115340.

93 R. Karthick and F. Chen, *Carbon*, 2019, **150**, 292–310.

94 J. Wang, Y. Mao, G. Li and H.-M. Yin, *Chem. Eng. J.*, 2022, **441**, 136014.

95 X. Guo, S. Zheng, G. Zhang, X. Xiao, X. Li, Y. Xu, H. Xue and H. Pang, *Energy Storage Mater.*, 2017, **9**, 150–169.

96 X. W. Wang, H. P. Guo, J. Liang, J. F. Zhang, B. Zhang, J. Z. Wang, W. B. Luo, H. K. Liu and S. X. Dou, *Adv. Funct. Mater.*, 2018, **28**, 1801016.

97 P. Srimuk, J. Lee, A. Tolosa, C. Kim, M. Aslan and V. Presser, *Chem. Mater.*, 2017, **29**, 9964–9973.

98 P. Srimuk, J. Lee, S. Fleischmann, S. Choudhury, N. Jäckel, M. Zeiger, C. Kim, M. Aslan and V. Presser, *J. Mater. Chem. A*, 2017, **5**, 15640–15649.

99 J. Lee, P. Srimuk, K. Aristizabal, C. Kim, S. Choudhury, Y. C. Nah, F. Mücklich and V. Presser, *ChemSusChem*, 2017, **10**, 3611–3623.

100 J. Lee, P. Srimuk, R. Zwingelstein, R. L. Zornitta, J. Choi, C. Kim and V. Presser, *J. Mater. Chem. A*, 2019, **7**, 4175–4184.

101 M. Torkamanzadeh, L. Wang, Y. Zhang, O. Z. Budak, P. Srimuk and V. Presser, *ACS Appl. Mater. Interfaces*, 2020, **12**, 26013–26025.

102 D. Sriramulu and H. Y. Yang, *Nanoscale*, 2019, **11**, 5896–5908.

103 X. Shen, L. Li, Y. Xiong, F. Yu and J. Ma, *J. Mater. Chem. A*, 2022, **10**, 10192–10200.

104 H. Zhang, A. Li, Y. Yuan, Y. Wei, D. Zheng, Z. Geng, H. Zhang, G. Li and F. Zhang, *Carbon Energy*, 2020, **2**, 656–674.

105 J. Chen, K. Zuo, B. Li, D. Xia, L. Lin, J. Liang and X.-Y. Li, *Sep. Purif. Technol.*, 2022, **304**, 122381.

106 J. Chen, K. Zuo, B. Li, J. Hu, W. Liu, D. Xia, L. Lin, J. Liang and X.-Y. Li, *Chem. Eng. J.*, 2022, **433**, 133781.

107 X. Shen, Y. Xiong, R. Hai, F. Yu and J. Ma, *Environ. Sci. Technol.*, 2020, **54**, 4554–4563.

108 M. Liang, L. Wang, V. Presser, X. Dai, F. Yu and J. Ma, *Adv. Sci.*, 2020, **7**, 2000621.

109 X. Shen, R. Hai, X. Wang, Y. Li, Y. Wang, F. Yu and J. Ma, *J. Mater. Chem. A*, 2020, **8**, 19309–19318.

110 J. Ma, Y. Cheng, L. Wang, X. Dai and F. Yu, *Chem. Eng. J.*, 2020, **384**, 123329.

111 B. Li, K. Sun, W. Xu, X. Liu, A. Wang, S. Boles, B. Xu, H. Hu and D. Yao, *Nano Res.*, 2022, DOI: 10.1007/s12274-022-4491-3.

112 S. Wang, Z. Li, G. Wang, Y. Wang, Z. Ling and C. Li, *ACS Nano*, 2022, **16**, 1239–1249.

113 J. Lei, Y. Xiong, F. Yu and J. Ma, *Chem. Eng. J.*, 2022, **437**, 135381.

114 L. Wu, M. Liu, S. Huo, X. Zang, M. Xu, W. Ni, Z. Yang and Y.-M. Yan, *Carbon*, 2019, **149**, 627–636.

115 G. Zhang, W. Li, Z. Chen, J. Long and C. Xu, *Carbon*, 2022, **187**, 86–96.

116 F. Ji, L. Wang, J. Yang, X. Wu, M. Li, S. Jiang, S. Lin and Z. Chen, *J. Mater. Chem. A*, 2018, **7**, 1768–1778.

117 L. Agartan, K. Hantanasirisakul, S. Buczek, B. Akuzum, K. A. Mahmoud, B. Anasori, Y. Gogotsi and E. C. Kumbur, *Desalination*, 2020, **477**, 114267.

118 K. Singh, Z. Qian, P. M. Biesheuvel, H. Zuilhof, S. Porada and L. C. P. M. D. Smet, *Desalination*, 2020, **481**, 114346.

119 B. Chen, A. Feng, K. Liu, J. Wu, Y. Yu and L. Song, *Ceram. Int.*, 2021, **47**, 3665–3670.

120 K. Singh, G. Li, J. Lee, H. Zuilhof, B. L. Mehdi, R. L. Zornitta and L. C. P. M. Smet, *Adv. Funct. Mater.*, 2021, **31**, 2105203.

121 Y. Sun, Y. Su, Z. Zhao, J. Zhao, M. Ye and X. Wen, *Chem. Eng. J.*, 2022, **443**, 136542.

122 X. Wen, M. Zhao, D. Zhang, X. Ma, Z. Lin and M. Ye, *Desalination*, 2019, **470**, 114117.

123 C. Hu, T. Wang, J. Dong, R. Liu, H. Liu and J. Qu, *Appl. Surf. Sci.*, 2018, **459**, 767–773.

124 Z. Zhao, J. Zhao, Y. Sun, M. Ye and X. Wen, *Chem. Eng. J.*, 2022, **429**, 132582.

125 K. Shen, S. Zhai, S. Wang, Q. Ru, X. Hou, K. S. Hui, K. N. Hui and F. Chen, *Batteries Supercaps*, 2021, **4**, 860–880.

126 J. Liu, J. Long, Z. Shen, X. Jin, T. Han, T. Si and H. Zhang, *Adv. Sci.*, 2021, **8**, 2004689.

127 H. Li and Y. J. Zhu, *Chem. – Eur. J.*, 2020, **26**, 9180–9205.

128 C. Hu, J. Dong, T. Wang, R. Liu, H. Liu and J. Qu, *Chem. Eng. J.*, 2018, **335**, 475–482.

129 W. Zhao, M. Ding, L. Guo and H. Y. Yang, *Small*, 2019, **15**, 1805505.

130 S. Vafakhah, L. Guo, D. Sriramulu, S. Huang, M. Saeedikhani and H. Y. Yang, *ACS Appl. Mater. Interfaces*, 2019, **11**, 5989–5998.

131 S. Vafakhah, M. Saeedikhani, S. Huang, D. Yan, Z. Y. Leong, Y. Wang, L. Hou, L. Guo, P. V. Y. Alvarado and H. Y. Yang, *J. Mater. Chem. A*, 2021, **9**, 10758–10768.

132 X. Wen, M. Zhao, Z. Zhao, X. Ma and M. Ye, *ACS Sustainable Chem. Eng.*, 2020, **8**, 7335–7342.

133 X. Wen, M. Zhao, M. Zhang, X. Fan and D. Zhang, *ACS Sustainable Chem. Eng.*, 2020, **8**, 1268–1275.

134 V. Consonni and A. M. Lord, *Nano Energy*, 2021, **83**, 105789.

135 S. P. Ratnayake, J. Ren, E. Colusso, M. Guglielmi, A. Martucci and E. D. Gaspera, *Small*, 2021, **17**, 2101666.

136 Y. Jayasree, U. Chalapathi, P. U. Bhaskar and V. S. Raja, *Appl. Surf. Sci.*, 2012, **258**, 2732–2740.

137 H. H. Kyaw, M. T. Z. Myint, S. Al-Harthi, A. A. H. Al-Muhtaseb and M. Al-Abri, *Sep. Purif. Technol.*, 2022, **281**, 119888.

138 C. Zhang, D. Wang, Z. Wang, G. Zhang, Z. Liu, J. Wu, J. Hu and G. Wen, *Energy Environ. Mater.*, 2023, **6**, e12276.

139 J. Wang, D. Zhang, X. Hu and T. Sun, *New J. Chem.*, 2022, **46**, 8679–8687.

140 X. Zhang and J. Dutta, *ACS Appl. Energy Mater.*, 2021, **4**, 8275–8284.

141 Y. Zhang, L. Ji, Y. Zheng, H. Liu and X. Xu, *Sep. Purif. Technol.*, 2020, **234**, 116124.

142 R. Li, D. Wu, J. Song, Y. He, W. Zhu, X. Wang, L. Wang, N. M. Dube and K. Jiang, *Desalination*, 2022, **540**, 115990.

143 X. Xu, T. Yang, Q. Zhang, W. Xia, Z. Ding, K. Eid, A. M. Abdullah, M. S. A. Hossain, S. Zhang, J. Tang, L. Pan and Y. Yamauchi, *Chem. Eng. J.*, 2020, **390**, 124493.

144 X. Zhang, E. A. Toledo-Carrillo, D. Yu and J. Dutta, *ACS Appl. Mater. Interfaces*, 2022, **14**, 40371–40381.

145 S. A. Hawks, M. R. Cerón, D. I. Oyarzun, T. A. Pham, C. Zhan, C. K. Loeb, D. Mew, A. Deinhart, B. C. Wood, J. G. Santiago, M. Stadermann and P. G. Campbell, *Environ. Sci. Technol.*, 2019, **53**, 10863–10870.

146 R. He, M. Neupane, A. Zia, X. Huang, C. Bowers, M. Wang, J. Lu, Y. Yang and P. Dong, *Adv. Funct. Mater.*, 2022, **32**, 2208040.

147 M. Liu, M. Xu, Y. Xue, W. Ni, S. Huo, L. Wu, Z. Yang and Y.-M. Yan, *ACS Appl. Mater. Interfaces*, 2018, **10**, 31260–31270.

148 M. R. Cerón, F. Aydin, S. A. Hawks, D. I. Oyarzun, C. K. Loeb, A. Deinhart, C. Zhan, T. A. Pham, M. Stadermann and P. G. Campbell, *ACS Appl. Mater. Interfaces*, 2020, **12**, 42644–42652.

149 Y. Li, Y. Liu, M. Wang, X. Xu, T. Lu, C. Q. Sun and L. Pan, *Carbon*, 2018, **130**, 377–383.

150 G. Zhu, H. Wang, H. Xu and L. Zhang, *J. Electroanal. Chem.*, 2018, **822**, 81–88.

151 L. Agartan, B. Akuzum, T. Mathis, K. Ergenekon, E. Agar and E. C. Kumbur, *Sep. Purif. Technol.*, 2018, **202**, 67–75.

152 C. Kim, P. Srimuk, J. Lee, S. Fleischmann, M. Aslan and V. Presser, *Carbon*, 2017, **122**, 329–335.

153 W. Kong, G. Wang, M. Zhang, X. Duan, J. Hu and X. Duan, *Desalination*, 2019, **459**, 1–9.

154 Y. Zhang, P. Ren, L. Wang, E. P. Yambou, S. Husmann and V. Presser, *Desalination*, 2022, **542**, 116053.

155 S. Duan, Y. Zhao, S. Jiang, Z. Yang, Y. Ju, C. Chen, L. Huang and F. Chen, *Chem. Eng. J.*, 2022, **442**, 136287.

156 D. Ahn, D. Kim, J. H. Park, N. Kim, E. Lim and C. Kim, *Desalination*, 2021, **520**, 115333.

157 W. Wei, X. Gu, R. Wang, X. Feng and H. Chen, *Nano Lett.*, 2022, **22**, 7572–7578.

158 J. Ai, J. Li, K. Li, F. Yu and J. Ma, *Chem. Eng. J.*, 2021, **408**, 127256.

159 M. Ding, S. Li, L. Guo, L. Jing, S. P. Gao, H. Yang, J. M. Little, T. U. Dissanayake, K. Li, J. Yang, Y. X. Guo, H. Y. Yang, T. J. Woehl and P. Y. Chen, *Adv. Energy Mater.*, 2021, **11**, 2101494.

160 J. Ma, L. Wang and F. Yu, *Electrochim. Acta*, 2018, **263**, 40–46.

161 Y. Cai, L. Zhang, R. Fang, Y. Wang and J. Wang, *Sep. Purif. Technol.*, 2022, **292**, 121019.

162 N. Liu, Y. Zhang, X. Xu and Y. Wang, *Dalton Trans.*, 2020, **49**, 6321–6327.

163 J. Xue, Q. Sun, Y. Zhang, W. Mao, F. Li and C. Yin, *ACS Omega*, 2020, **5**, 10995–11004.

164 M. S. Zoromba, M. H. Abdel-Aziz, M. Bassyouni, S. Gutub, D. Demko and A. Abdelkader, *ACS Sustainable Chem. Eng.*, 2017, **5**, 4573–4581.

165 D. Song, W. Guo, T. Zhang, P. Lu, A. Guo, F. Hou, X. Yan and J. Liang, *Surf. Innovations*, 2018, **7**, 1–29.

166 J. Feng, S. Xiong and Y. Wang, *Sep. Purif. Technol.*, 2019, **213**, 70–77.

167 S. Vafakhah, G. J. Sim, M. Saeedikhani, X. Li, P. V. Y. Alvarado and H. Y. Yang, *Nanoscale Adv.*, 2019, **1**, 4804–4811.

168 B. Cai and A. Eychmüller, *Adv. Mater.*, 2019, **31**, 1804881.

169 J. Liu, Y. Zhao, X. Huang, Y. Zhou, K.-H. Lam, D. Y. W. Yu and X. Hou, *Chem. Eng. J.*, 2022, **435**, 134839.

170 X. Wu, S. Zhou, Y. Li, S. Yang, Y. Xiang, J. Jiang, Z. Liu, D. Fan, H. Zhang and L. Zhu, *J. Alloys Compd.*, 2021, **858**, 157744.

171 P. X. Hou, F. Zhang, L. Zhang, C. Liu and H. M. Cheng, *Adv. Funct. Mater.*, 2022, **32**, 2108541.

172 Y. Song, W. Zou, Q. Lu, L. Lin and Z. Liu, *Small*, 2021, **17**, 2007600.

173 Z. Yao, L. Zhou, H. Yin, X. Wang, D. Xie, X. Xia, C. Gu and J. Tu, *Small*, 2019, **15**, 1904433.

174 M. B. Kale, R. A. Borse, A. G. A. Mohamed and Y. Wang, *Adv. Funct. Mater.*, 2021, **31**, 2101313.

175 T. Chu, S. Park and K. Fu, *Carbon Energy*, 2021, **3**, 424–439.

176 Z. Jin, Y. Li, K. Yu, L. Liu, J. Fu, X. Yao, A. Zhang and Y. He, *Adv. Sci.*, 2021, **8**, 2101394.

177 J. G. Gamaethiralalage, K. Singh, S. Sahin, J. Yoon, M. Elimelech, M. E. Suss, P. Liang, P. M. Biesheuvel, R. L. Zornitta and L. C. P. M. D. Smet, *Energy Environ. Sci.*, 2021, **14**, 1095–1120.

178 R. Chen, T. Sheehan, J. L. Ng, M. Brucks and X. Su, *Environ. Sci.: Water Res. Technol.*, 2019, **6**, 258–282.